

1 **Improved Prediction of Dimethyl Sulfide (DMS) Distributions in the**
2 **NE Subarctic Pacific using Machine Learning Algorithms**

3 Brandon J. McNabb¹ & Philippe D. Tortell^{1,2}

4 ¹Department of Earth, Ocean and Atmospheric Sciences, University of British Columbia, Vancouver, BC V6T 1Z4,
5 Canada

6 ²Department of Botany, University of British Columbia, Vancouver, BC V6T 1Z4, Canada

7 *Correspondence to:* Brandon J. McNabb (bmcnabb@eoas.ubc.ca)

8 **Abstract.** Dimethyl sulfide (DMS) is a volatile biogenic gas with the potential to influence regional climate as a
9 source of atmospheric aerosols and cloud condensation nuclei (CCN). The complexity of the oceanic DMS cycle
10 presents a challenge in accurately predicting sea-surface concentrations and sea-air fluxes of this gas. In this study,
11 we applied machine learning methods to model the distribution of DMS in the NE Subarctic Pacific (NESAP), a
12 global DMS hot-spot. Using nearly two decades of ship-based DMS observations, combined with satellite-derived
13 oceanographic data, we constructed ensembles of 1000 machine-learning models using two techniques, random
14 forest regression (RFR) and artificial neural networks (ANN). Our models dramatically improve upon existing
15 statistical DMS models, capturing up to 62% of observed DMS variability in the NESAP and demonstrating notable
16 regional patterns that are associated with mesoscale oceanographic variability. In particular, our results indicate a
17 strong coherence between DMS concentrations, sea surface nitrate (SSN) concentrations, photosynthetically active
18 radiation (PAR) and sea surface height anomalies (SSHA), suggesting that NESAP DMS cycling is primarily
19 influenced by heterogenous nutrient availability, light-dependent processes and physical mixing. Based on our
20 model output, we derive summertime, sea-air flux estimates of 1.16 ± 1.22 Tg S in the NESAP. Our work
21 demonstrates a new approach to capturing spatial and temporal patterns in DMS variability, which is likely
22 applicable to other oceanic regions.

23 **1 Introduction**

24 Dimethyl sulfide (DMS), a volatile biogenic gas, is an important component of the marine sulfur cycle.
25 This molecule is an important substrate for specific methylotrophic bacteria (Vila-Costa et al., 2006; Lidbury et al.,
26 2016; Green et al., 2011; Hatton et al., 2012), with a recognized importance to marine microbial metabolism (Vila-
27 Costa et al., 2006) and food web interactions (Nevitt, 2008). Moreover, DMS constitutes the largest fraction of
28 bulk non-sea salt (NSS) sulfate emissions to the atmosphere (Bates et al., 1992; Ksionzek et al., 2016), where it is
29 rapidly oxidized to form aerosols that act as cloud condensation nuclei (CCN; Charlson et al., 1987; Hegg et al.,
30 1991; Korhonen et al., 2008), potentially influencing regional albedo and climate (Charlson et al., 1987; Ayers and
31 Caaney, 2007). Given the ecological roles of DMS and its potential influence on global climate, substantial research
32 has focused on characterizing the dynamics of this compound in seawater. This work has revealed considerable
33 complexity in the oceanic DMS cycle, which has limited the development of simple predictive algorithms
34 describing its spatial and temporal variability.

35 Oceanic DMS production and loss are tightly linked with the biological cycling of the related metabolites
36 dimethyl sulfoniopropionate (DMSP) and dimethyl sulfoxide (DMSO). DMS is believed to be primarily derived

37 from the cleavage of DMSP (Kiene and Linn, 2000), but it can also be cycled through biological DMSO reduction
38 (Spiese et al., 2009) and oxidation (Lidbury et al., 2016), and abiotically by light-dependent reactions (del Valle et
39 al., 2007; Royer et al., 2016). DMS cycling is influenced by a suite of environmental and ecological factors,
40 including release from phytoplankton cells into the dissolved pool via grazing (Dacey and Wakeham, 1986), viral
41 lysis (Malin et al., 1998), or exudation. Oxidative stress generated by other variables such as temperature (Kirst et
42 al., 1991), salinity (Dickson and Kirst, 1987), UV radiation (Kinsey et al., 2016), and nutrient limitation (Bucciarelli
43 et al., 2013; Spiese & Tatarkov, 2014) may also enhance the cycling of DMSP and DMSO, which may regulate
44 DMS concentrations through cascading oxidative pathways (Sunda et al., 2002). Finally, variability in surface wind
45 fields can modulate the rates of DMS sea-air exchange, providing a significant source of heterogeneity in surface
46 water DMS concentrations (Royer et al., 2016). These examples illustrate the complex non-linearity of the oceanic
47 DMS cycle.

48 Over the past two decades, a number of approaches have been developed to model DMS distributions at
49 both global (Bock et al., 2021; Galí et al., 2018; Simó and Dachs, 2002; Vallina and Simó, 2007) and regional
50 (Watanabe et al., 2007) scales. These models have been largely based on linear regression techniques estimating
51 DMS concentrations using one or two predictors. To date, these studies have focused on a number of variables,
52 including ratio of chlorophyll a (Chl-a) to mixed layer depth (MLD) (Simó and Dachs, 2002), sea surface
53 temperature (SST) and nitrate (SSN) (Watanabe et al., 2007), solar radiation dose (SRD) (Vallina and Simó, 2007),
54 photosynthetically active radiation (PAR) and modelled DMSP concentrations (Galí et al., 2018). Some of these
55 models have demonstrated reasonably good performance at global scales, but their predictive power is generally
56 diminished at regional scales (Herr et al., 2019), failing to accurately resolve important smaller-scale features
57 (Belviso et al., 2003; Nemcek et al., 2008; Royer et al., 2015; Tortell, 2005b).

58 In recent years, machine-learning algorithms have been increasingly used to derive predictions for non-
59 linear oceanic systems. For example, these methods have been successfully applied to describe the spatial and
60 temporal patterns of global methane flux (Weber et al., 2019), nitrous oxide dynamics (Yang et al., 2020), and
61 carbon export (Roshan and DeVries, 2017). To our knowledge, only two studies have thus far applied machine-
62 learning to describe DMS distributions, with one study focused on the Arctic (Humphries et al., 2012) and the other
63 exploring a global domain (Wang et al., 2020). Despite producing algorithms with reasonable predictive skill, these
64 two studies found limited success in resolving the underlying relationships driving DMS variability. This was
65 partially due to a reliance on indirect sensitivity tests assessing the importance of predictor variables, and also,
66 potentially, from the large-scale averaging applied to the underlying data fields ($1 \times 1^\circ$; 111 km^2). Analyses at higher

67 spatial resolution may reveal mesoscale (roughly 20-200 km) and sub-mesoscale (roughly 1-20 km) patterns that
68 would otherwise be obscured, thereby increasing predictive strength.

69 Machine learning algorithms require large datasets for the training and testing process. Traditionally, DMS
70 measurements were based on time-consuming ship-board analysis of discrete samples, resulting in sparse data
71 coverage over much of the oceans. More recently, the development of several automated DMS measurement
72 systems (Royer et al., 2014; Saltzman et al., 2009; Tortell, 2005a) has provided marine DMS observations at a
73 significantly higher resolution, yielding greater spatial and temporal data coverage. These new datasets potentially
74 enable new insights into small-scale and regional patterns in oceanic DMS distributions, as well as the
75 characterization of oceanic DMS ‘hot-spots’. The northeast subarctic Pacific (NESAP) is a region of notably high
76 DMS concentrations (Lana et al., 2011), with localized DMS accumulation in both highly productive coastal
77 upwelling regimes, and off-shore, iron-limited waters ((Herr et al., 2019; Asher et al., 2017). Several factors have
78 been proposed to account for the elevated DMS production in the NESAP, including increased primary productivity
79 driven by nutrient entrainment and upwelling along coastal fronts (Asher et al., 2017), a dominance of high-DMSP
80 producing prymnesiophytes and dinoflagellates in offshore waters, elevated microbial degradation of DMSP to
81 DMS (Steiner et al., 2012; Royer et al., 2010), and the stimulation of DMS production in response to oxidative
82 stress in low iron waters (Sunda et al., 2002; Herr et al., 2020). Although multiple studies have examined empirical
83 relationships between DMS and various oceanographic factors in the NESAP (Watanabe et al., 2007; Herr et al.,
84 2019; Asher et al., 2017, 2011), these have all reported low predictive skill based on simple linear correlation
85 approaches. To date, machine-learning approaches have not been applied to describe DMS distributions specifically
86 in this region.

87 Here, we present an approach to modelling summertime NESAP DMS concentrations and sea-air fluxes
88 using ensemble random forest regression (RFR) and artificial neural network (ANN) machine-learning algorithms.
89 Our statistical models leverage field observations of DMS collected across the NESAP between 1997 to 2017 to
90 generate a summertime DMS climatology mapped at a higher spatial resolution than previous efforts (Simó and
91 Dachs, 2002; Vallina and Simó, 2007; Galí et al., 2018; Watanabe et al., 2007; Humphries et al., 2012; Wang et
92 al., 2020). This new modelling approach represents a significant improvement over previous methods, and predicts
93 regional DMS distributions that are coherent with underlying patterns of oceanographic variability. Most notably,
94 the modelled DMS concentrations and sea-air fluxes can be explained, to a large extent, by regional and mesoscale
95 patterns in nutrient supply and physical mixing dynamics. Based on the output of our models, we present
96 summertime sea-air flux estimates in close agreement with previous studies (Herr et al., 2019; Lana et al., 2011),
97 further highlighting the importance of the NESAP as a globally-significant sulfur source to the atmosphere.

98 2 Methods

99 2.1 Data

100 A combination of data sources was used in training our machine-learning models to build a summertime
101 DMS climatology. For this study, we restricted DMS measurements to the months of June, July and August between
102 1997 to 2017 in the NESAP (43-60°N, 147-122°W). A total of 26,201 data points were obtained from the NOAA
103 PMEL repository (<https://saga.pmel.noaa.gov/dms/>; last accessed: February 3, 2021), including measurements
104 derived from purge and trap gas chromatography and membrane inlet mass spectrometry. The DMS data were
105 binned to a monthly resolution, regardless of year, and averaged into 0.25 x 0.25° grid cells.

106 Predictor data used to build our machine-learning models included the following variables derived from
107 the NASA Aqua MODIS satellite at level L3 monthly 0.042° resolution (R2018.0): sea surface temperature (SST),
108 the ratio of normalized fluorescence line height to chlorophyll a (nFLH:Chl-a), instantaneous and daily observed
109 photosynthetically active radiation (iPAR and PAR, respectively), particulate inorganic carbon (PIC), the
110 absorption of gelbstof and detritus at 433 nm ($a_{\text{cdm}}(443)$), and diffuse attenuation coefficients at 490nm (K_d).
111 Satellite-based PIC is considered as a proxy for the abundance of coccolithophores and other calcified
112 phytoplankton (Franklin et al., 2010), whereas the $a_{\text{cdm}}(443)$ product is considered a proxy for chromophoric
113 dissolved organic matter (CDOM) (Nelson & Siegel, 2013), which is thought to be an important photosensitizer of
114 DMS (see Sect. 4.1). For observations prior to 2004, data were from either SeaWiFS (0.083° resolution) or Terra
115 MODIS (0.042° resolution) when SeaWiFS data were unavailable (*e.g.* nFLH and iPAR). As described below, K_d
116 and PIC were later excluded from the final models (see Sect. 2.6), as they didn't improve predictive skill.

117 The following predictor variables were also used: 6-day averaged sea surface height anomalies (SSHA)
118 derived from the TOPEX/Poseidon satellites at 0.17° resolution; Level L4 ESA Sentinel-3 Copernicus monthly-
119 averaged 0.25° wind speeds; net primary productivity (NPP) from the Vertically-Generalized Production Model
120 (VGPM; Behrenfeld & Falkowski, 1997) at monthly 0.25° resolution; sea surface nitrate from the 2018 World
121 Ocean Atlas at monthly 1° resolution (Garcia et al., 2019); and mixed-layer depth (MLD) and sea surface salinity
122 (SSS) from the MIMOC climatology at 0.5° resolution (Schmidtke et al., 2013). Except for MIMOC data, all
123 predictors were restricted in time to the corresponding years of DMS sampling (1997 to 2017). Net community
124 productivity (NCP) was estimated from the algorithm of Li & Cassar, (2016; using NPP and SST). As with DMS
125 observations, predictor data were interpolated to a 0.25 x 0.25° average monthly resolution using linear radial basis
126 interpolation functions. Interpolation was constrained to the oceanic region by masking out land pixels using
127 ETOPO2 bathymetric (0.033° resolution) binned at 0.25 x 0.25° resolution. We note that each of these data sources

128 are likely to have inherent uncertainties associated with either their collection or processing. Data sources can be
 129 found in Table 1.

130

131 **Table 1. Data sources and spatial and temporal resolution of predictor variables used to develop the RFR and ANN algorithms. Data**
 132 **processing levels are indicated where relevant. All variables were used as predictors (excluding bathymetry) and post-processed to**
 133 **monthly-averaged, 0.25° resolution (see sections 2.1-2.2).**

Variable	Spatial Resolution (°)	Temporal Resolution	Source	Level
Sea Surface Temperature (SST)	0.042	6-Day Average	SeaWiFS/AquaTERRA (1997-2003) or AquaMODIS(2004-2017): https://oceancolor.gsfc.nasa.gov/l3/	3
Chlorophyll-Normalized Fluorescence (nFLH:Chl-a)	0.042	Monthly	SeaWiFS/AquaTERRA (1997-2003) or AquaMODIS (2004-2017): https://oceancolor.gsfc.nasa.gov/l3/	3
Instantaneous Photosynthetically Active Radiation (iPAR)	0.042	Monthly	SeaWiFS/AquaTERRA (1997-2003) or AquaMODIS (2004-2017): https://oceancolor.gsfc.nasa.gov/l3/	3
Daily Photosynthetically Active Radiation (PAR)	0.042	Monthly	SeaWiFS/AquaTERRA (1997-2003) or AquaMODIS (2004-2017): https://oceancolor.gsfc.nasa.gov/l3/	3
Particulate Inorganic Carbon (Calcite; PIC)	0.042	Monthly	SeaWiFS/AquaTERRA (1997-2003) or AquaMODIS (2004-2017): https://oceancolor.gsfc.nasa.gov/l3/	3
Absorption of Gelbstof and Detritus at 433 nm ($a_{cdm}(443)$)	0.042	Monthly	SeaWiFS/AquaTERRA (1997-2003) or AquaMODIS (2004-2017): https://oceancolor.gsfc.nasa.gov/l3/	3
Diffuse Attenuation Coefficients at 490 nm (K_d)	0.042	Monthly	SeaWiFS/AquaTERRA (1997-2003) or AquaMODIS (2004-2017): https://oceancolor.gsfc.nasa.gov/l3/	3
Sea Surface Height Anomalies (SSHA)	0.17	Monthly	TOPEX/Poseidon: https://podaac.jpl.nasa.gov/dataset/SEA_SURFACE_HEIGHT_ALT_GRID_S_L4_2SATS_5DAY_6THDEG_V_J_PL1812	4
Monthly Wind Speeds	0.25	Monthly	ESA Sentinel-3 Copernicus: https://resources.marine.copernicus.eu/?option=com_csw&view=details&product_id=WIND_GLO_PHY_CLIMAT_E_L4_REP_012_003	N/A

Net Primary Productivity (NPP)	0.25	Monthly	Vertically-Generalized Production Model (VGPM): http://www.science.oregonstate.edu/ocean.productivity/	N/A
Sea Surface Nitrate (SSN)	1	Monthly	World Ocean Atlas 2018 (WO18): https://www.ncei.noaa.gov/access/world-ocean-atlas-2018/	N/A
Mixed Layer Depth (MLD)	0.5	Monthly	MIMOC Climatology: https://www.pmel.noaa.gov/mimoc/	N/A
Sea Surface Salinity (SSS)	0.5	Monthly	MIMOC Climatology: https://www.pmel.noaa.gov/mimoc/	N/A
Bathymetry	0.033	N/A	ETOPO2: https://rda.ucar.edu/datasets/ds759.3/	N/A

136 2.2 Machine-learning models

137 We compared the performance of random forest regression (RFR) and artificial neural network (ANN)
 138 models at the regional scale. The RFR algorithm is built upon decision tree models, which operate by iteratively
 139 generating decision rule nodes that dictate which branch the tree will progress through in the next iteration. The
 140 RFR model builds an ensemble, or “forest”, of these trees, where each tree is trained on a bootstrapped (*i.e.*
 141 randomly subsampled) set of predictors, and the resulting predictions are averaged among the trees to reduce
 142 overfitting to noise (Brieman, 2001). In contrast, the ANN model is built as a fully connected network of nodes, or
 143 “neurons”, in which each neuron consists of an activation function and is connected to other neurons by iteratively-
 144 determined weights (Gardner and Dorling, 1998). Both algorithms are advantageous because they make no prior
 145 assumptions on the data distributions and can fit non-linear data (Brieman, 2001; Gardner and Dorling, 1998).

146 Both our ANN and RFR models followed a similar design to Weber et al. (2019). Our ANNs were built
 147 using a feed-forward framework consisting of a single input node, two hidden layers each consisting of 30 neurons
 148 (using a sigmoidal activation function), and a single output layer (using a linear activation function). A Bayesian
 149 L2 (Ridge) regularization parameter was tuned to minimize overfitting and the L-BFGS algorithm was used to
 150 solve for weights (Byrd et al., 1995). Each individual decision tree within the RFR was trained using the standard
 151 CART algorithm (Brieman, 2001) and constrained to a max depth of 25 decision splits, the simplest configuration
 152 determined to perform well and minimize overfitting. These models were built using the Scikit-Learn (v0.24.2)
 153 implementation of the ANN (“MLPRegressor”) and RFR (“RandomForestRegressor”) algorithms in Python 3.8
 154 (see Code Availability).

155 In both cases, the models were built as an ensemble of either 1000 individual decision trees or individual
 156 networks to minimize bias in predictions. The input data were randomly divided for use in model training (80%)
 157 and external testing (20%). Although RFR is not sensitive to large differences in predictor variance, predictor data
 158 were standardized in both models by normalization to their respective mean and standard deviation. Additionally,
 159 we applied an inverse hyperbolic sine (IHS) transformation to the DMS data prior to training (Weber et al., 2019).
 160 Testing results indicated that IHS yielded slightly better performance than the more traditional logarithmic
 161 transformations for both of our models.

162 2.3 Sea-to-air fluxes

163 Sea-air DMS fluxes (F_{DMS} , $\mu\text{mol m}^{-2} \text{d}^{-1}$) were calculated from the monthly-averaged observed and
164 modelled DMS values for June, July and August. F_{DMS} was calculated using the gas transfer velocity (k , cm hr^{-1})
165 following the modified approach of Webb et al. (2019):

$$166 F_{DMS} = k(DMS)(0.24) \quad (1)$$

167 where the factor of 0.24 converts to the values to daily fluxes. The gas transfer velocity has typically been calculated
168 using a non-linear parameterization (Nightingale et al., 2000), but recent work has suggested a linear
169 parameterization is more appropriate for DMS (Bell et al., 2013; Blomquist et al., 2017; Zavarisky et al., 2018).
170 Since satellite-derived predictors are used to build our models, we calculated the gas transfer velocity using the
171 linear Goddijn-Murphy et al. (2012) k parameterization, which is both derived from satellite altimeter data and
172 normalized to a Schmidt number of 660:

$$173 k_{w,660} = 2.1U_{10} - 2.8 \quad (2)$$

174 Where U_{10} is the wind speed (m s^{-1}) at 10 m above sea surface.

175 Regional summertime fluxes (\bar{F}_{DMS} , Tg) were calculated as the average ($\pm\text{SD}$) quantity of DMS-sulfur
176 emitted over 92 days (June, July and August) through the area of the mapped study region ($1.28 \times 10^7 \text{ km}^2$ or 85.0%
177 of the total bounded area).

178 2.4 Comparison against existing algorithms

179 Simple linear regression (LR) and multiple linear regression (MLR) models were built for comparison
180 against the machine-learning algorithms. We also tested the performance of our RFR and ANN models against the
181 published algorithms of Simó & Dachs (2002), Watanabe et al. (2007), Vallina & Simó, (2007), and Galí et al.
182 (2018) (hereafter referred to as SD02, W07, VS07, and G18, respectively). Solar radiation dose, SRD, used in the
183 VS07 algorithm was calculated using MLD as described by Vallina & Simó (2007):

$$184 SRD = \frac{PAR}{K_d \times MLD} \times (1 - e^{-K_d \times MLD}) \quad (4)$$

185 Each of the four algorithms was assessed using both their original coefficients and coefficients tuned to
186 our NESAP dataset using nonlinear least-squares optimization at both 0.25° and 1° spatial resolution (Table 2). In
187 each case, the algorithms were run using the same monthly-averaged predictors used to develop the RFR and ANN
188 ensembles (see Sec. 2.1). Predictors were spatially matched to either the full DMS dataset (*i.e.* all monthly averaged
189 DMS observations) or to only the Testing partitioned dataset (see Sec. 2.2) for direct comparison with the RFR and
190 ANN ensemble performance (Fig. 2, Table 2).

191 2.5 Controls on DMS variability

192 Principal component analysis (PCA) was applied to assess the relationships between DMS and the nine
193 predictors used to build the RFR and ANN ensembles. Additionally, non-parametric Spearman rank correlations
194 were calculated between each variable and both the modelled and observed DMS concentrations. Correlation
195 analysis was also extended to assess the role of taxonomy on predicted DMS concentrations, using the outputs of
196 a chlorophyll-a based taxonomic algorithm by Hirata et al. (2011) with NESAP-tuned coefficients (Zeng et al.,
197 2018).

198 2.6 Sensitivity Tests and Predictor Selection

199 To inform our selection of grid size, we assessed the performance of both the RFR and ANN models using
200 grid cells ranging from 0.25 to 5° (Fig. 1). From this analysis, we found that model accuracy was highest at 0.25°
201 resolution (see Sect. 3.1). Smaller grid sizes would presumably further improve model accuracy, but at a
202 significantly higher computational cost.

203 We also tested the influence of other biological predictor variables on the performance of the RFR and
204 ANN models, using either NCP, NPP, Chl-a, or PIC. These sensitivity tests indicated no significant difference
205 between the various biological predictor variables, although accuracy was slightly reduced when PIC was used.
206 We therefore selected NCP as the biological predictor variable within our model framework. We also removed K_d
207 as a predictor variable after further sensitivity testing indicated that its exclusion slightly improved results.

208 The inclusion of nFLH:Chl-a represents a proxy for iron limitation (see Sect. 4.1). However, fluorescence
209 yields corrected for non-photochemical quenching (NPQ) have been suggested to yield a better iron limitation
210 proxy than nFLH:Chl-a (Behrenfeld et al., 2009). We therefore calculated NPQ-corrected fluorescence yields (φ_f)
211 by:

$$212 \quad \varphi_f = \frac{nFLH}{Chl - \alpha \times \alpha \times S} \times \frac{iPAR}{iPAR} \quad (5)$$

213 where $\alpha = 0.0147 \times Chl - \alpha^{-0.316}$ and $S = 100 \text{ mW cm}^{-2} \mu\text{m}^{-1} \text{ sr}^{-1} \text{ m}$ as described by Behrenfeld et al. (2009). Our
214 tests indicated nFLH:Chl-a yielded slightly improved performance overall, whereas φ_f decreased both models'
215 performance. We therefore retained nFLH:Chl-a and excluded φ_f in our final model design.

216

217

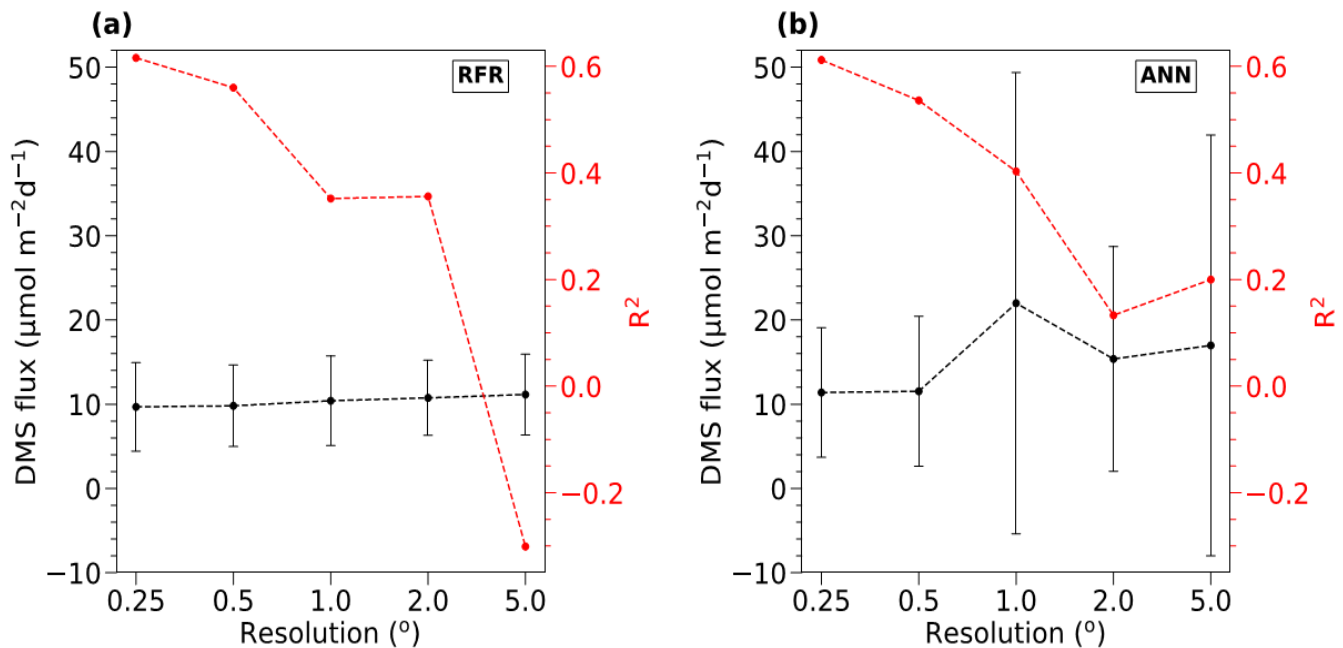


Fig. 1. Sensitivity of RFR and ANN models to grid size resolution. DMS fluxes (black) and R^2 values (red) derived from sensitivity tests of (a) RFR and (b) ANN models to pixels resolutions of 0.25-5°. The negative R^2 values observed at the lowest resolution (largest grid cells) indicate that the predicted values explain less variance than the overall mean of the dataset.

3 Results

3.1 Model evaluation

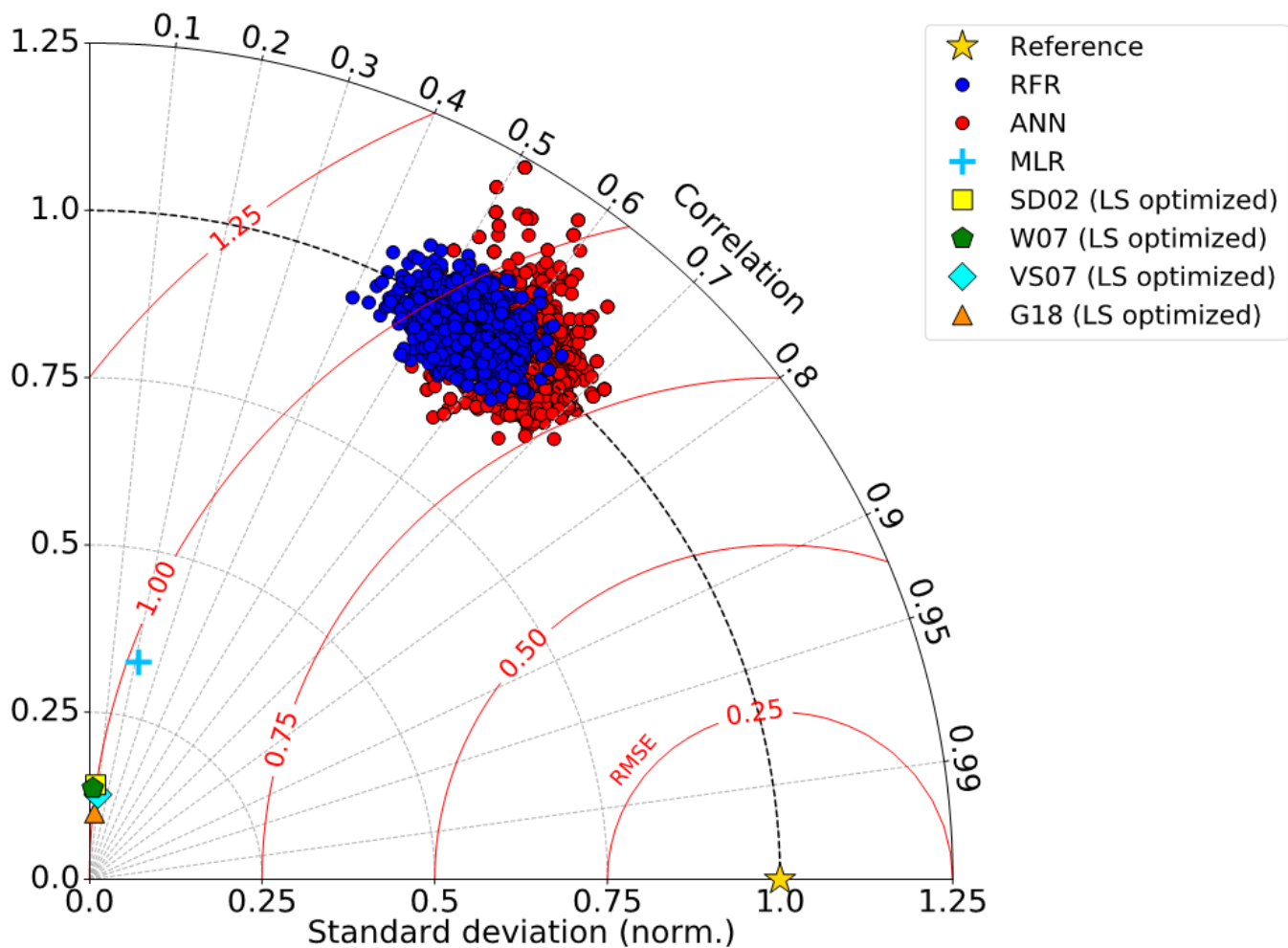
To benchmark the performance of our RFR and ANN models, we first evaluated the predictive skill of four existing empirical DMS algorithms (SD02, W07, VS07, & G18), in addition to simple and multiple linear regression models. Previous studies have demonstrated that these empirical algorithms show strong predictive skill ($R^2=0.53-0.84$) over large scales and in some oceanic regions (Simó and Dachs, 2002; Galí et al., 2018; Watanabe et al., 2007), but significantly poorer performance in the NESAP (Herr et al., 2019). Consistent with these results, we found that the SD02, W07, VS07, and G18 did not accurately predict NESAP DMS distributions, even with regionally tuned coefficients improving performance (Fig. 2, $R^2=0-0.01$ at $0.25 \times 0.25^\circ$; Table 2, $r=-0.15-0.36$). We also found that simple and multiple linear regressions performed poorly, yielding virtually no explanatory power for surface water DMS distributions in the NESAP ($R^2=0-0.05$; Fig. 2, 3).

Table 2. Performance of statistical DMS algorithms on NESAP DMS observations binned to monthly 1° and 0.25° resolution. Pearson correlation coefficients (r) and root mean square error (nM) are obtained from the

SD02, VS07, W07 and G18 algorithms (see 2.4) using either their original published coefficients or coefficients derived from non-linear least squares optimization. Algorithm performance is evaluated using either the full monthly-binned observational dataset or using the Testing partitioned dataset (see Sec. 2.2).

		SD02		VS07		W07		G18	
		Original	Optimized	Original	Optimized	Original	Optimized	Original	Optimized
1°		r = -0.09	r = 0.17	r = -0.03	r = 0.03	r = -0.10	r = 0.07	r = 0.02	r = 0.16
All data		RMSE = 18.03	RMSE = 4.82	RMSE = 6.67	RMSE = 4.96	RMSE = 11.74	RMSE = 4.83	RMSE = 6.77	RMSE = 4.84
1°		r = -0.22	r = 0.36	r = 0.11	r = 0.20	r = -0.03	r = 0.02	r = -0.15	r = 0.30
Testing dataset		RMSE = 19.09	RMSE = 3.34	RMSE = 5.36	RMSE = 3.47	RMSE = 10.46	RMSE = 3.47	RMSE = 6.19	RMSE = 3.40
0.25°		r = -0.05	r = 0.12	r = -0.09	r = 0.11	r = -0.09	r = 0.04	r = 0.06	r = 0.09
All data		RMSE = 11.02	RMSE = 7.84	RMSE = 9.57	RMSE = 7.88	RMSE = 13.02	RMSE = 7.80	RMSE = 8.42	RMSE = 7.88
0.25°		r = -0.03	r = 0.07	r = -0.09	r = 0.10	r = -0.06	r = 0.04	r = 0.04	r = 0.08
Testing dataset		RMSE = 9.79	RMSE = 6.79	RMSE = 8.60	RMSE = 6.79	RMSE = 12.02	RMSE = 6.78	RMSE = 7.47	RMSE = 6.80

239



240

241 **Fig. 2. Taylor Diagram showing comparative performance metrics of each individual Random Forest Regression (RFR)**
 242 **and Artificial Neural Network (ANN) model (1000-model ensembles) against multiple linear regression (MLR) and**
 243 **other statistical DMS models (See sections 2.1 and 2.4). The Pearson correlation coefficients (“Correlation”; outer**
 244 **radius), root mean squared error (“RMSE”; red radial contours), and standard deviations (SDs; grey radial contours**
 245 **from origin) are all computed with respect to the observed DMS samples after inverse hyperbolic sine (IHS)**
 246 **transformation. The reference of a perfect model fit is shown with a gold star. SDs of the model outputs are normalized**
 247 **to the SDs of the DMS observations. RMSE represents a normalized trigonometric derivation from both the correlation**
 248 **coefficients and normalized SDs. Performance of the SDO2, W07, VS07, and G18 algorithms reported here are**
 249 **calculated using regionally tuned coefficients to the NESAP derived from non-linear least-squares optimization (see**
 250 **section 2.4).**

251 Relative to other published modelling approaches, both the RFR and ANN models dramatically improved
 252 the representation of NESAP DMS variability, achieving significantly higher predictive accuracy (Fig. 2, 3). The
 253 collective ensembles of both the RFR and ANN models yielded strong performance, explaining up to 62% of the
 254 observed DMS variability ($R^2=0.61-0.62$; Fig. 3). For individual models within the ensembles, the ANN method

provided slightly better results ($R^2=0.16-0.50$), compared to the individual RFR models ($R^2=0.16-0.43$). However, predicted DMS concentrations and sea-air fluxes derived from the ANN ensembles were more sensitive to the spatial resolution used, although the predictive accuracy of both models degraded significantly with coarser resolutions (Fig. 1).

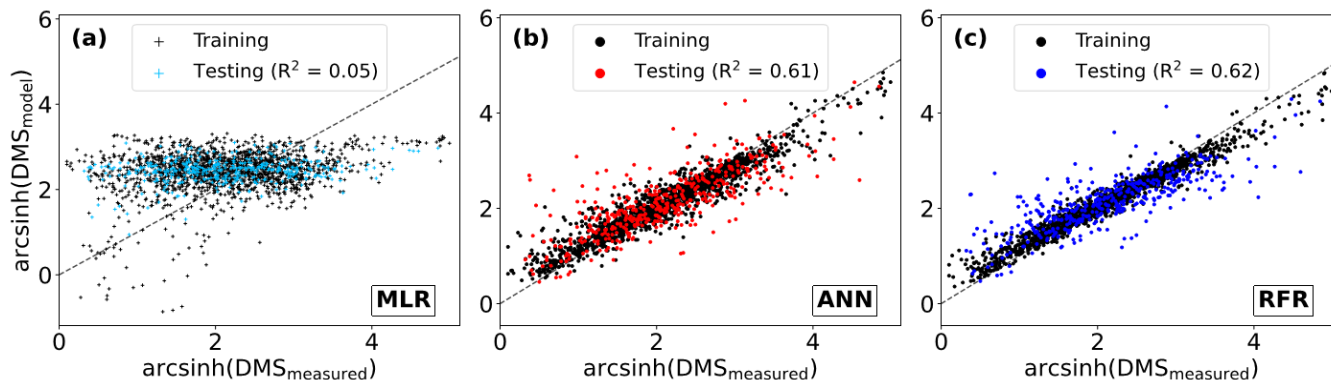


Fig. 3. Performance of three modelling approaches in predicting observed DMS distributions; (A) multiple linear regression (MLR) (B) ensemble of Artificial Neural Networks (ANN) and (C) ensemble of Random Forest Regression (RFR). For consistency, all predictions are partitioned by the Training and Testing datasets used to build the ensembles (see section 2.2). Model performance (R^2) is computed only for the Testing dataset predictions. The dashed line demonstrates a 1:1 relationship. Modelled DMS concentrations depicted range from 0.4-84.3 (RFR, nM) and 0.3-74.6 (ANN, nM).

3.2 DMS distributions and sea-air fluxes

In both the RFR and ANN methods, the predicted spatial distribution of DMS was generally consistent with observations (Fig. 4a,c,d). The average model derived DMS concentrations was 4.0 ± 2.1 nM and 4.7 ± 3.0 nM (mean \pm SD) for the RFR and ANN ensemble models, respectively, with a similar range from 0.3 to 84.3 nM. In both models, the highest DMS concentrations were largely constrained to coastlines and within the Alaska Gyre adjacent to the Aleutian Islands (Fig. 4b-c, 8C). The greatest discrepancy between DMS concentrations from the two models was observed in these regional ‘hotspots’, where the ANN models emphasize high DMS within the Alaska gyre, while the RFR models emphasize elevated coastal DMS concentrations (Fig. 4b). On average, the models deviated from each other by 0.49 nM, with the greatest offsets observed in an area of particularly sparse DMS observations in the Alaska Gyre (Fig. 4a,b). Future observational data in this region should help improve model agreement.

June – August

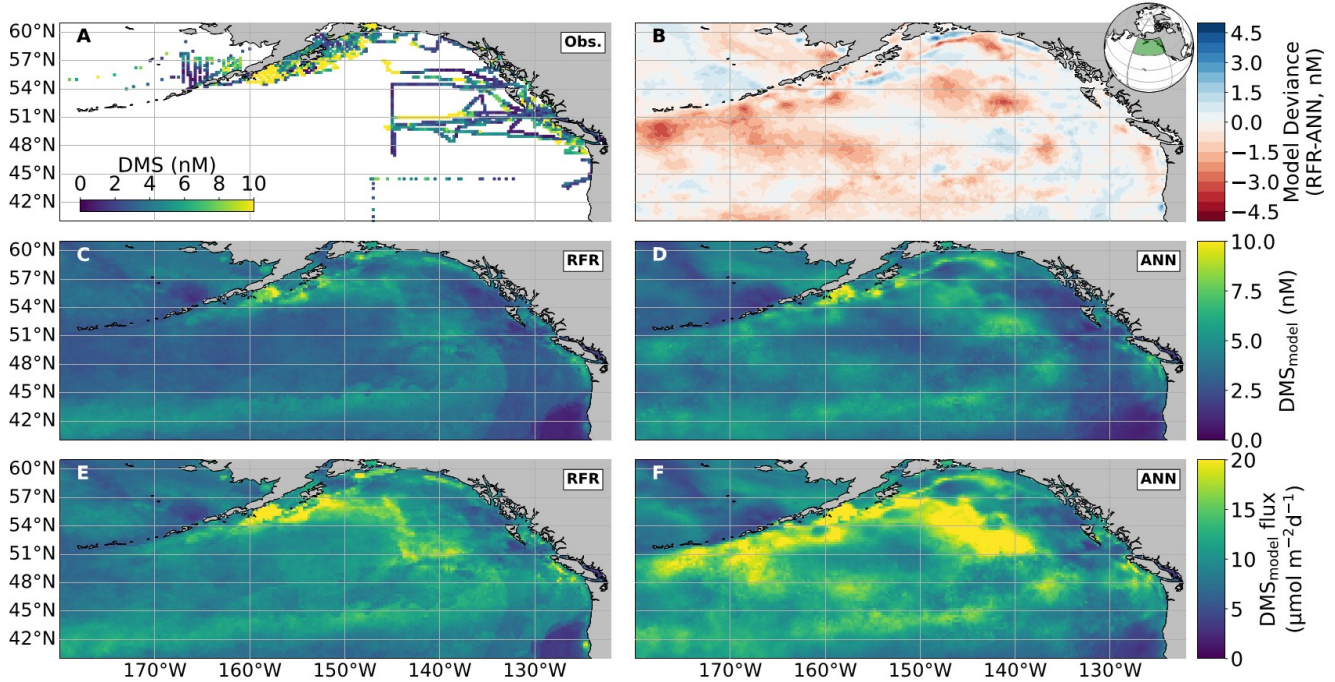


Fig. 4. Predicted maps of sea surface DMS concentrations and sea-air fluxes. (a) Ship-based observations of mean summertime (June-August) DMS concentrations used to construct the predictive models. (b) Differences between the (c) Random Forest Regression (RFR) and (d) Artificial Neural Network (ANN) ensemble predicted DMS concentrations. (e,f) DMS sea-air fluxes derived from the predicted DMS concentrations. Colormap ranges are restricted to illustrate trends, with <1% of DMS data exceeding the colorbar limits. The inset map in (b) shows the NESAP study region as a shaded green patch in a global orthographic projection.

Sea-air DMS fluxes (Fig. 4e,f) derived from ANN predictions were 18% higher, on average, than RFR predictions, largely due to higher predicted values in the Alaska Gyre (Fig. 4d-e, Table 3). The distribution of ANN sea-air fluxes was also closer to ship-based observations (Fig. 5). Predicted regional fluxes ranged from 0.8 to 167 $\mu\text{mol m}^{-2} \text{d}^{-1}$ between the two models (Fig. 4e,f, 5), with the highest predicted DMS emissions in August, when derived sea-air fluxes were approximately 1.6 to 2-fold greater than in June and July (Table 3). Our models yielded a summertime integrated sea-air flux of $1.16 \pm 1.22 \text{ Tg DMS-derived sulfur}$, which is consistent with the Lana et al. (2011) climatological estimate of $1.64 \pm 0.51 \text{ Tg}$ (Table 3).

Table 3. Monthly and mean summertime NESAP sea-air DMS fluxes. Total cumulative fluxes of DMS-derived sulfur (Tg, mean \pm SD) are calculated from the Random Forest Regression (RFR) and Artificial Neural Network (ANN) model predictions (based on an ensemble of 2000 models). Total cumulative NESAP sea-air flux derived from the Lana et al. (2011) climatology is shown for comparative purposes.

Summertime Sulfur Emissions

	RFR	ANN	This Study	Lana et al. (2011)
	$\mu\text{mol m}^{-2} \text{ d}^{-1}$	$\mu\text{mol m}^{-2} \text{ d}^{-1}$	Tg S	Tg S
June	8.0 ± 5.3	8.0 ± 5.5	0.29 ± 0.19	0.59 ± 0.24
July	8.2 ± 3.5	9.7 ± 4.6	0.33 ± 0.14	0.41 ± 0.16
August	12.7 ± 3.5	16.5 ± 4.6	0.54 ± 0.25	0.65 ± 0.25
June-August	9.7 ± 2.8	11.4 ± 4.0	1.16 ± 0.35	1.64 ± 0.51

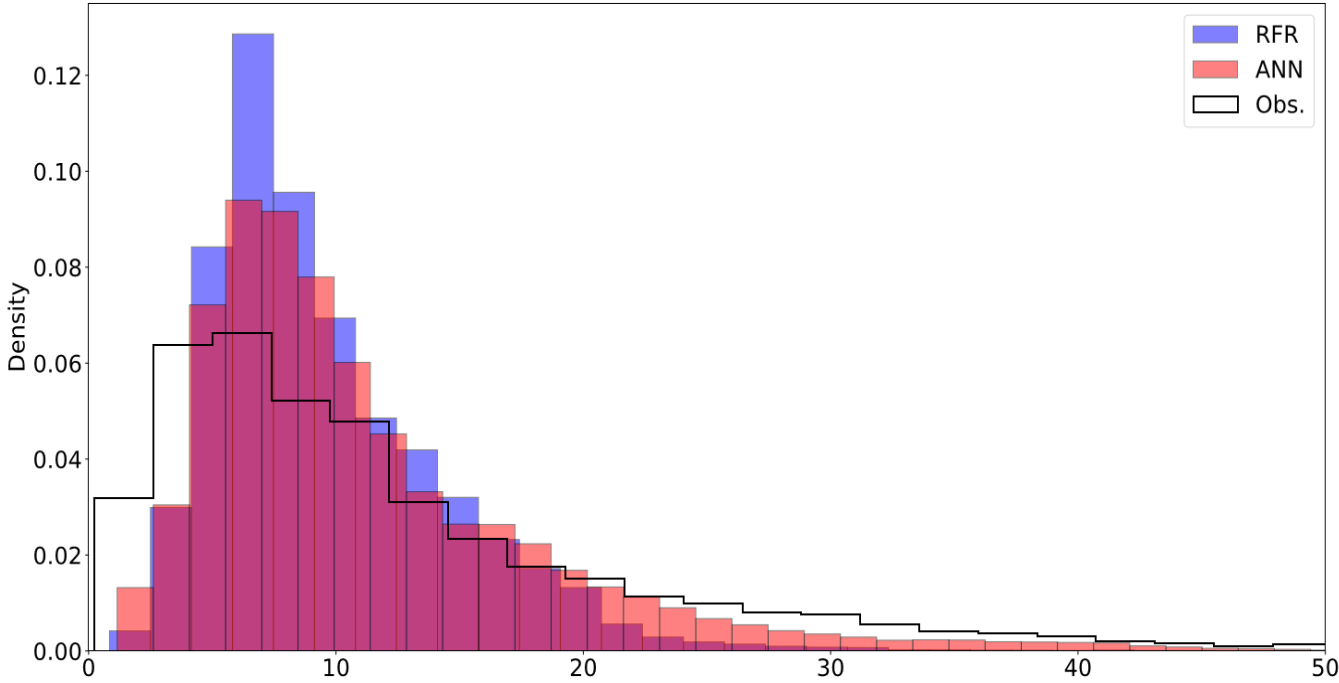
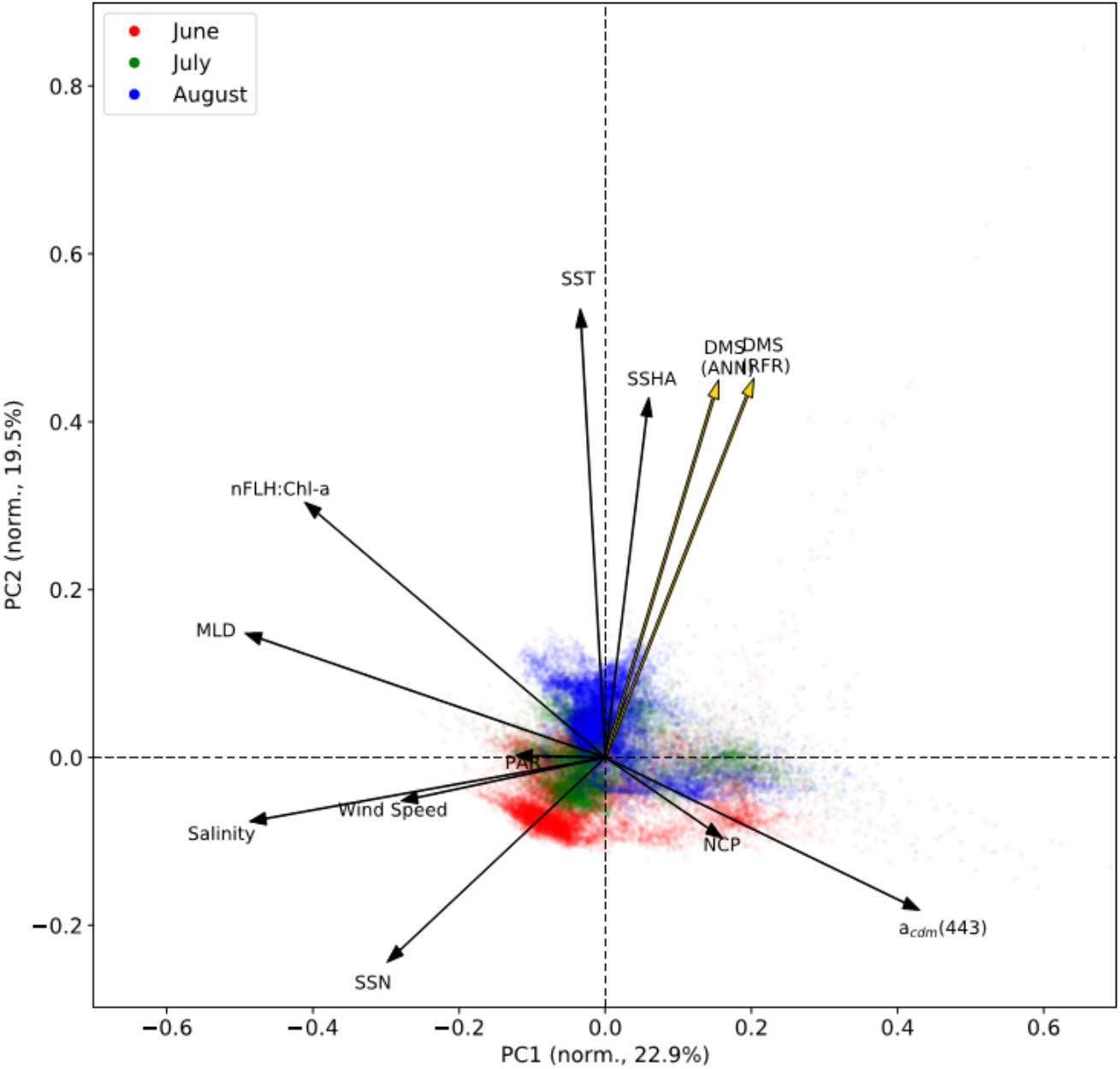


Fig. 5. Histograms of DMS sea-air flux distributions derived from the 1000-model ensemble random forest regression (RFR) and artificial neural network (ANN) predictions as well as cruise observations (Obs.). The sample sizes of both models are equivalent ($n= 49,632$) and are significantly higher than the observational dataset ($n=2063$). Note that the distribution is restricted to show trends, with a maximum flux of 238 nM (Obs.). The upper tail (>50 nM) consists of only 2.9% (Obs.) and $<0.1\%$ (both RFR and ANN) of the values. Note that the ANN better predicts the upper tail of DMS observations greater than 20 nM.

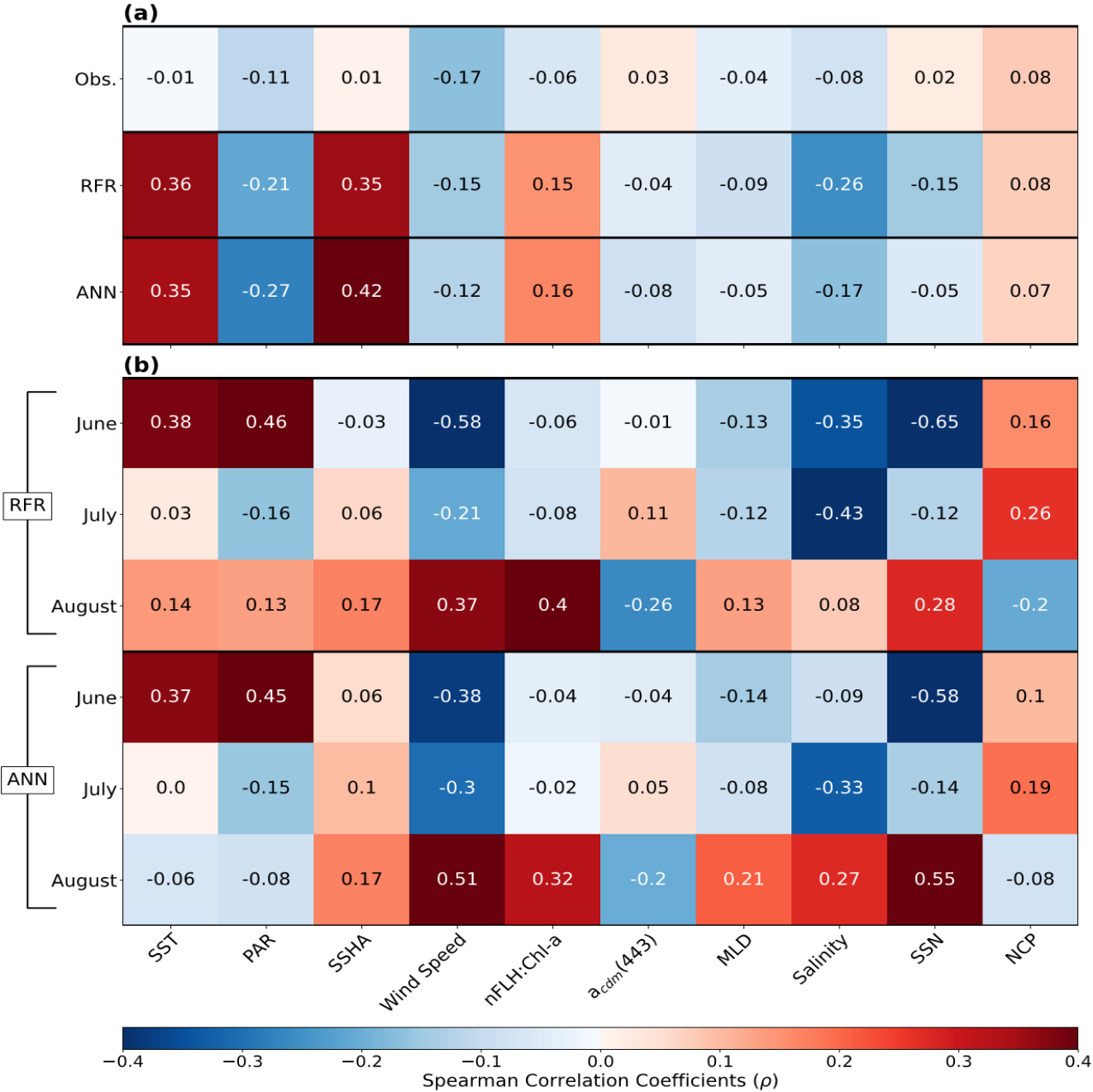
309 3.4 Drivers of DMS variability

310 In addition to modelling the spatial and temporal distribution of surface water DMS in the NESAP, we
311 examined the influence of different oceanographic variables as model predictors. As expected based on previous
312 work (Herr et al., 2019), no single predictor was found to exert a dominant control on modelled DMS distributions
313 from either the RFR or ANN models (Fig. 6, 7). Rather, the relationship between DMS and other oceanographic
314 variables exhibited significant region-specific patterns. One of the most compelling regional signatures was the
315 apparent relationship between DMS and SSHA. In both models, we found significant positive correlations between
316 DMS and SSHA ($\rho=0.35$, 0.42 for RFR and ANN, respectively) across the full spatial domain, with a particularly
317 notable relationship along the northern Alaskan coastline (Fig. 8, 9). Here, strong winds (Fig. 9j-l), coupled with
318 the northeastern Alaska current flow, produce two characteristic oceanographic features in the NESAP: strong,
319 semi-permanent mesoscale eddies collectively referred to as the Haida, Sitka and Yakutat eddies (Fig. 8a), and the
320 formation of the high nutrient, low chlorophyll (HNLC) Alaska Gyre (Fig. 8c; Okkonen et al., 2001; Whitney et
321 al., 2005). Both the monthly (Fig. 9a-i) and summertime-averaged (Fig. 8a,b) RFR and ANN-derived DMS
322 concentrations are low where these downwelling eddies form. In contrast, elevated DMS concentrations were
323 associated with the negative SSHA coastal upwelling areas (Fig. 8a,b), where phytoplankton productivity is
324 stimulated by nutrient inputs into the mixed layer.



326

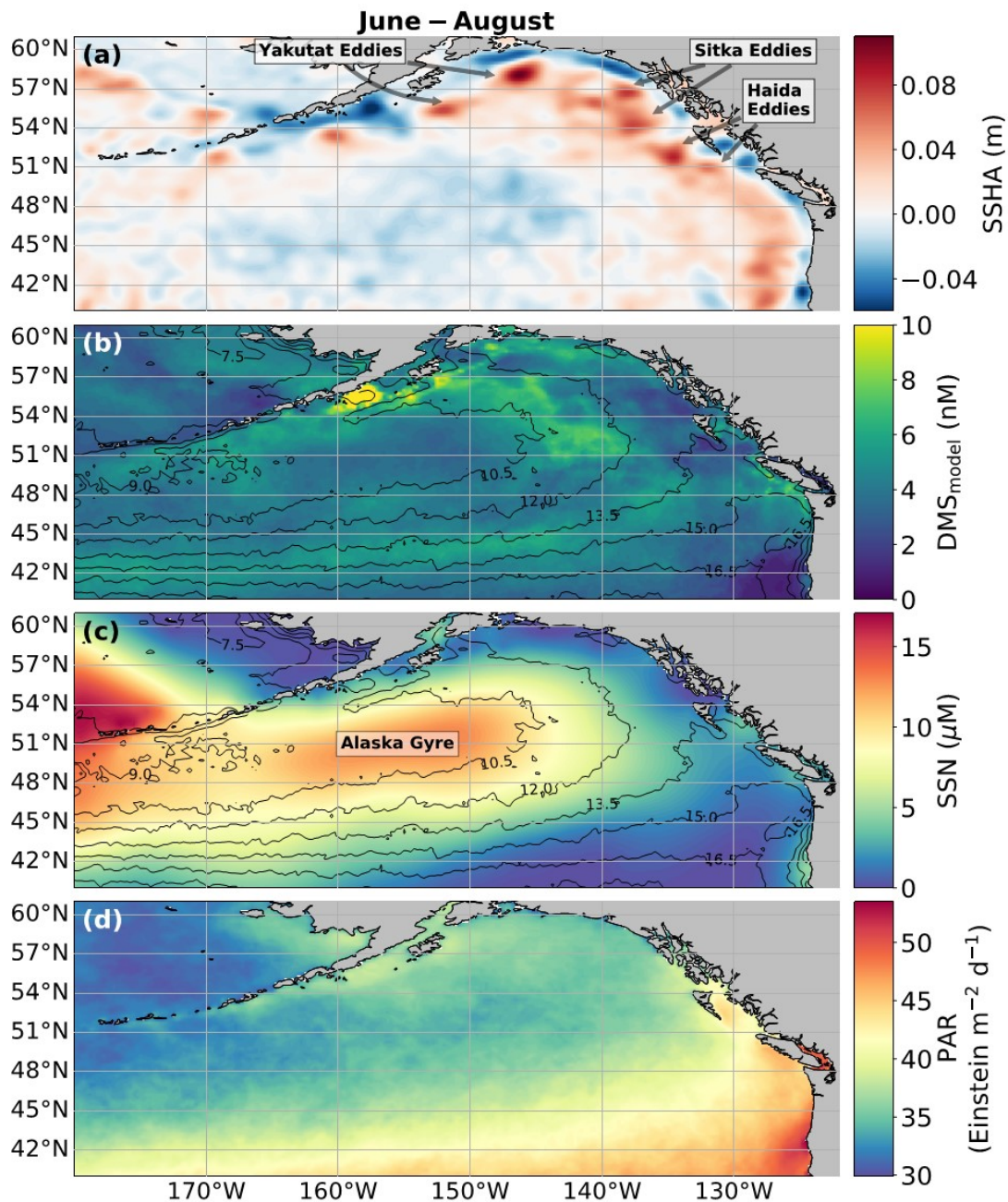
327 **Fig. 6. Principal Component Analysis (PCA) showing the relationships between variables used to construct the**
328 **predictive algorithms. Eigenvectors (arrows) are superimposed over the principal components (PCs; data points) for**
329 **the first two significant modes obtained from PCA. PCs are normalized and clustered by month (June-August, see**
330 **legend for colors), while the eigenvectors are grouped by ensemble model predictions (gold) and nine predictor**
331 **variables (black). The percentage of variance explained by each mode is indicated along the axes.**



333

334 **Fig. 7. Heatmap of Spearman rank correlations (ρ). (a) Correlations of pooled data (June-August) for DMS**
335 **observations (Obs.), RFR and ANN predictions per variable. (b) Correlations per month for the RFR and ANN DMS**
336 **predictions. All model correlations are computed on the 1000-model ensembles.**

337 Modelled DMS concentrations also significantly correlated with hydrographic frontal patterns. We found
338 significant correlations between DMS and SST ($\rho=0.36$, 0.35 for RFR and ANN, respectively) which suggested
339 the central Alaska Gyre and offshore of Vancouver Island are areas of elevated DMS variability (Fig. 8b). Both
340 models predict high DMS levels in the northern frontal zone of the gyre (140°W - 145°W) between the 10.5 and
341 12°C isotherms and the southern frontal zone between (42°N - 45°N) between the 13.5 and 15°C isotherms (Fig.
342 8b,c). By comparison, our models suggest that DMS concentrations are predominantly low in relation to high sea
343 surface nitrate (SSN) concentrations within the HNLC gyre (Fig. 8, 9). As discussed below, the relationship
344 between DMS and macronutrient concentrations in the HNLC waters of the central Gulf of Alaska could indicate
345 an important role for iron limitation as a controlling factor in the DMS cycle. The presence of elevated summer
346 nutrients in offshore waters is taken as a proxy for iron limitation, which increases over the course of the summer
347 growing season.



348

349

350

351

352

353

354

Fig. 8. Physical drivers of summertime (June-August) NESAP DMS distributions. (a) Sea surface height anomalies (SSHA), (b) predicted DMS concentrations derived from the mean of all 2000 RFR and ANN machine learning models, (c) sea surface nitrate (SSN) and (d) photosynthetically active radiation (PAR). Contours in (b,c) show sea surface temperature (SST) isotherms. Coherent features of elevated sea-surface height indicate the presence of mesoscale eddies, whereas nearshore low SSHAs features reveal areas of upwelling. Colormaps ranges are restricted to illustrate trends with <1% of data exceeding the colorbar limits.

355 Other variables appear to exhibit a more localized or minimal influence on DMS cycling. For instance,
356 both NCP and DMS are elevated in productive nearshore waters, but NCP generally correlates weakly with both
357 RFR- and ANN-derived DMS concentrations ($p=0.08$, 0.07 for RFR and ANN, respectively). It should be noted,
358 however, the empirically-derived NCP estimates may carry more uncertainty than other predictors obtained from
359 direct satellite observations (Li and Cassar, 2016). Similarly to NCP, modelled phytoplankton taxonomic
360 composition (Hirata et al., 2011; Zeng et al., 2018) was not significantly correlated with predicted DMS
361 concentrations ($p<0.1$). Although strong, persistent winds appear to sustain low DMS concentrations off the coast
362 of Oregon and Vancouver Island (Fig. 9), wind speeds only weakly correlate with DMS overall for the region ($p=-$
363 0.15 and -0.12 for RFR and ANN, respectively). Additionally, high PAR in these areas correspond with low DMS
364 concentrations (Fig. 6d) and there is an overall negative correlation between PAR and DMS for the region (Fig. 6,
365 7; $p=-0.21$ and -0.27 for RFR and ANN, respectively). Finally, despite hypothesized links between DMS cycling
366 and iron limitation in the NESAP (Levasseur et al., 2006; Merzouk et al., 2006; Royer et al., 2010), nFLH:Chl-a
367 ratios (taken as a proxy for phytoplankton iron stress; Behrenfeld et al., 2009; Westberry et al., 2013) did not exhibit
368 any coherent spatial patterns, and only weakly correlated to our modelled DMS concentrations ($p=0.15$ and $p=0.16$
369 for RFR and ANN, respectively).

370

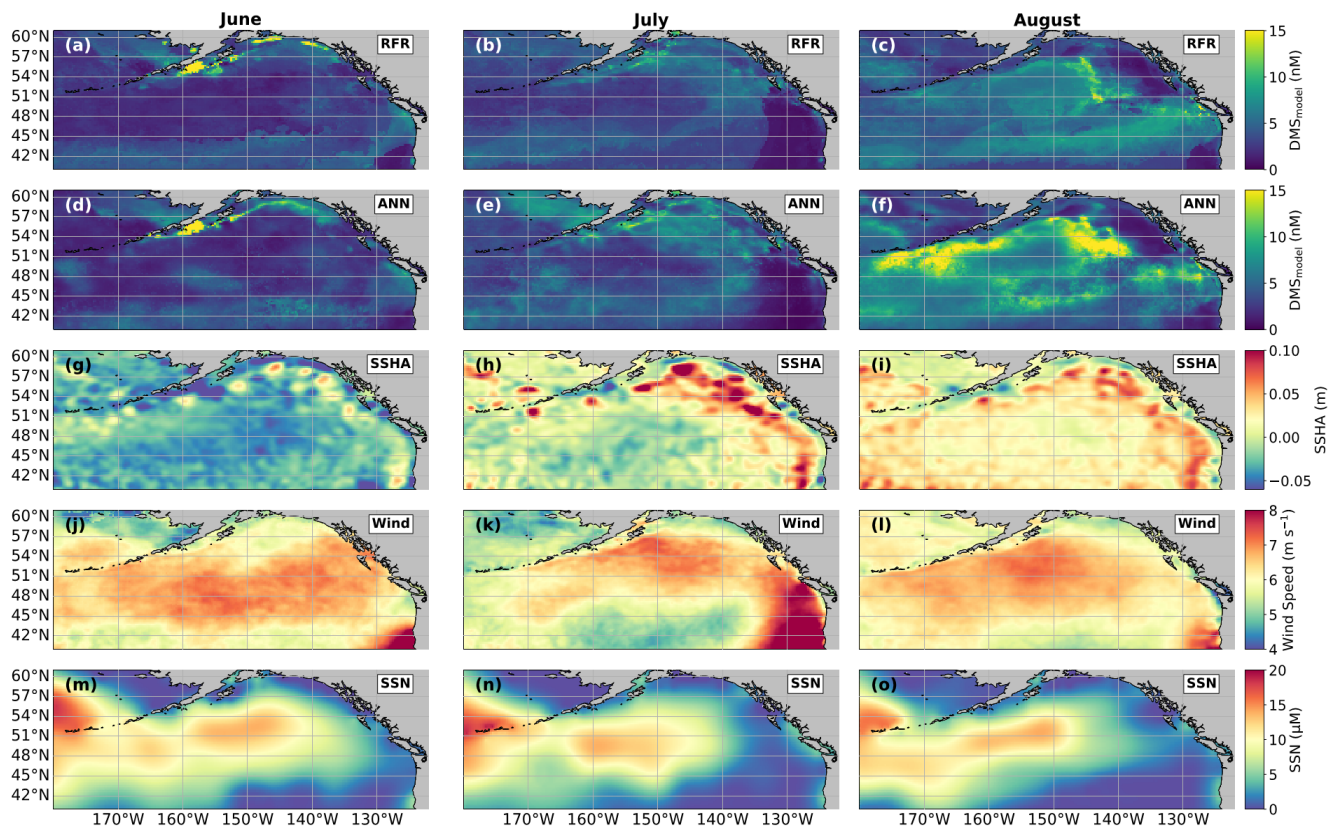


Fig. 9. Predicted spatial and temporal (June-August) DMS distribution in relation to underlying oceanographic variables. DMS concentrations predicted from (a-c) the Random Forest Regression (RFR) and (d-f) the Artificial Neural Network (ANN) ensemble models are mapped alongside the monthly-averaged (g-i) sea surface height anomalies (SSHA), (j-l) wind speeds (Wind), and (m-o) sea surface nitrate (SSN) for each month. Colormap ranges are restricted to illustrate trends, with at most 1.5% of the data beyond the colorbar limits.

4 Discussion

The relative sparsity of DMS data in many oceanic regions and the complexity of DMS cycling have limited previous attempts to model oceanic distributions of this compound (Simó and Dachs, 2002; Vallina and Simó, 2007; Galí et al., 2018; Watanabe et al., 2007; Herr et al., 2019). Taking advantage of expanding data resources, we employed a new approach to statistically describe DMS distributions in the NESAP. Our results show that both our RFR and ANN models substantially improved predictive strength over traditional empirical approaches (Fig. 2, 3), while identifying several key DMS relationships and regional patterns across the NESAP (Fig. 8, 9). Although our statistical approach does not directly elucidate the underlying mechanisms driving these relationships, and not all variability in predictors may be captured at the single spatial scale used here, we can nonetheless make some

386 reasonable inductive inferences. These inferences are discussed below, along with the implications of the improved
387 predictive performance observed here.

388 **4.1 Relationships with other oceanographic variables**

389 Among the more prominent spatial relationships we observed was the coherence between predicted DMS
390 concentrations and SST, and the negative correlation between predicted DMS concentrations and sea surface nitrate
391 (SSN) within and surrounding the Alaska Gyre (Fig. 6-9). Notably, regional SSN, NCP and Chl-a distributions did
392 not vary appreciably inside versus outside the gyre, and these variables were poorly correlated with DMS
393 concentrations ($r=-0.02$, $\rho=0.08$ with NCP, $r=0.09$, $\rho=-0.12$ with Chl-a). This suggests that the patterns in surface
394 DMS across the Alaska Gyre were not simply driven by changes in phytoplankton biomass or productivity. The
395 DMS-nitrate relationship may be partially explained by the so-called sulfur overflow hypothesis (Stefels, 2000),
396 which suggests that nutrient-limited phytoplankton increase DMSP production and its subsequent cleavage to
397 DMS, in order to regulate intracellular sulfur quotas when protein synthesis is limited (Hatton & Wilson, 2007;
398 Kinsey et al., 2016; Simó & Vila-Costa, 2006; Spiese & Tatarkov, 2014; Stefels, 2000). This mechanism may help
399 explain the higher predicted DMS concentrations at the northern extent of the Alaska Gyre, where SSN
400 concentrations begin to decrease (Fig. 6). Nutrient-dependent effects may also be important in explaining seasonal
401 variability, as the DMS-nitrate relationship becomes positive in August as phytoplankton growth becomes
402 increasingly nutrient limited (Fig. 7b).

403 The apparent relationship between DMS and nitrate could also result indirectly from the underlying effects of
404 iron limitation. Excess summertime nitrate concentrations are taken as evidence for iron limitation in the NESAP
405 (Boyd and Harrison, 1999; Boyd et al., 2004; Martin and Fitzwater, 1988; Whitney et al., 2005). Under iron-limiting
406 conditions, DMS is thought to function, together with DMSP and DMSO, as part of an antioxidant response to
407 oxidative stress (Sunda et al., 2002). This hypothesis suggests that iron limitation should stimulate net production
408 of DMS and DMSP (Bucciarelli et al., 2013; Sunda et al., 2002), which is inconsistent with the overall negative
409 dependence predicted between DMS and SSN (Fig. 8b,c).

410 Satellite-based, chlorophyll-normalized fluorescence has been suggested as an additional proxy for iron
411 limitation. Low iron conditions can lead to both a reduction in photosystem I relative to photosystem II (Strzepek
412 and Harrison, 2004), and an apparent increase in energetically-decoupled light harvesting complexes (Allen et al.,
413 2008; Behrenfeld & Milligan, 2013), resulting in elevated fluorescence-to-chlorophyll a ratios (nFLH:Chl-a)
414 (Westberry et al., 2013). To our knowledge, this proxy has not been widely investigated with respect to DMS
415 cycling. In our analysis, we found that nFLH:Chl-a ratios, and the NPQ-corrected fluorescence yields (ϕ_f), exhibited

only weak positive correlations with the RFR and ANN predicted DMS concentrations (Fig. 6, 7). Moreover, neither of these metrics exhibited coherent spatial patterns with predicted DMS concentrations, suggesting a limited role for iron in driving spatial patterns of DMS cycling within the NESAP. However, it is important to note the potential temporal mismatch between our monthly DMS predictions and these more instantaneous metrics of iron limitation, which reflect short-term physiological changes (days to weeks; Behrenfeld et al., 2009; Westberry et al., 2019) that depend on sporadic iron loading (*e.g.* aerosol deposition; Mahowald et al., 2009). Indeed, both natural and artificial iron-fertilization events have thus far been detected from satellite-derived nFLH:Chl-a at daily resolution (Westberry et al., 2013), in contrast to the monthly-averaged data used here. Therefore, modelling frameworks utilizing shorter temporal scales may find a clearer connection between DMS cycling and iron limitation using the chlorophyll-a fluorescence proxy.

Beyond nutrient limitation effects, ambient light fields are believed to exert significant direct and indirect effects on DMS cycling (del Valle et al., 2007). At the community level, high irradiance may inhibit bacterial consumption of DMS (Slezak et al., 2001; Toole et al., 2006; Lizotte et al., 2012), while covarying changes in mixing and high irradiance can induce transient selectivity for high-light acclimated species and influence the proportion of high DMS/P producers within assemblages (Galí et al., 2013; Vance et al., 2013). Ultraviolet radiation has been noted to induce high DMS production and turnover through a proposed cascading oxidation pathway, which acts to remove harmful reactive oxygen species (Sunda et al., 2002; Archer et al., 2010). In contrast, more recent evidence has indicated the potential for elevated DMS production in the NESAP from the reduction of DMSO due to light-induced oxidative stress over diurnal cycles (Herr et al., 2020). Although our modelled DMS concentrations exhibited an overall negative correlation with PAR (Fig. 6, 7a), monthly correlations indicate a stronger positive correlation between DMS and PAR in June, where the summer solstice drives high irradiance. In contrast, July and August exhibit much weaker negative correlations as the summer bloom declines (Fig. 7b). These results provide indirect evidence that light-induced oxidative stress, possibly coupled with inhibition of microbial DMS consumption, may influence regional NESAP DMS distributions, particularly early in the summer.

The overall negative association of DMS and incident light (Fig. 6, 7a) may also indicate a role for photolysis in DMS loss through (del Valle et al., 2007). Since DMS does not have strong light absorption properties, the presence of photosensitisers is necessary for the abiotic photooxidation of DMS (Brimblecombe and Shooter, 1986). To account for this process, our models incorporated nitrate (SSN) and a_{cdm} (as a proxy for CDOM; Nelson & Siegel, 2013), both of which are thought to be dominant photosensitisers of DMS in marine systems (Taalba et al., 2013; Bouillon and Miller, 2004, 2005; Galí et al., 2016). In the NESAP, nitrate appears to exert a stronger influence than CDOM on the apparent quantum yields (AQY) of DMS (Bouillon and Miller, 2004). In

support of this, our results suggest a stronger negative dependence of predicted DMS concentrations on nitrate compared to CDOM within the NESAP, particularly in June when irradiance is high (Fig. 6, 7). We acknowledge, however, that the DMS-nitrate relationship likely also reflects physiological impacts of nutrient limitation, as discussed above. Nonetheless, our results are consistent with elevated rates of DMS photo-oxidation in the nitrate-replete, low iron waters of the Alaska Gyre, where photolysis may drive strong DMS oxidation and explain the low predicted DMS concentrations (Fig. 8, 9). Further *in situ* work will be required to resolve the relative contributions of these biotic and abiotic processes to DMS cycling within these areas.

Among all the statistical relationships we observed, perhaps the most striking was the association of DMS variability with SSHA, particularly along the Alaskan coast and in relation to mesoscale eddies (Okkonen et al., 2001; Whitney et al., 2005; Fig. 8, 9). To our knowledge, only one other study has linked SSHA to DMS within the NESAP. Herr et al., (2019) demonstrated contrasting positive and negative correlations between DMS and SSHA in offshore and coastal waters, respectively, in general agreement with our results. Presently, the underlying mechanisms explaining the relationship between SSHA and DMS cycling remain unclear, yet it is likely that physical mixing processes are important. For example, enhanced biological production is known to be stimulated by eddy re-supply of iron and macronutrients via vertical advection and diffusion (Whitney et al., 2005; Bailey et al., 2008). These nutrient supply processes would also be expected to influence DMS cycling, as outlined above. Elevated abundances of high DMS-producers within anticyclonic eddies with positive sea surface height anomalies have been noted in the Sargasso Sea (Bailey et al., 2008), while eddy-induced vertical transport likely supplements nearshore, current-driven upwelling that can also resupply iron into the coastal waters of the NESAP (Cullen et al., 2009; Freeland et al., 1984). In addition, eddy propagation can allow cross-shelf transport, distributing micronutrients to offshore waters (Fiechter and Moore, 2012), potentially contributing to the apparent elevated DMS concentrations in the outer Alaska gyre between the 10.5 and 12°C isotherms (Fig. 8). These mixing and transport mechanisms could partially explain the influence of elevated productivity in driving increased nearshore and northern NESAP DMS concentrations (Fig. 4, 7-9), representing a novel source of DMS variability in this region.

The taxonomic composition of plankton assemblages is also a likely source of variability influencing DMS cycling. Significant changes to DMS production and consumption rates within the NESAP are expected in response to variable microbial and phytoplankton taxonomy (Vila-Costa et al., 2006; Lidbury et al., 2016; Sheehan and Petrou, 2020). Such taxonomic variability may, in turn, reflect transient community composition shifts in response to mixing (Bailey et al., 2008), nitrate (Bouillon and Miller, 2004), and iron availability (Levasseur et al., 2006; Merzouk et al., 2006). The monthly averaging used in our data processing removes autocorrelation associated with

individual sampling expeditions (Wang et al., 2020), but it may preclude capturing these transient taxonomic responses. For instance, coccolithophores are believed to influence DMS cycling in the NESAP (Herr et al., 2019; Asher et al., 2011), yet monthly-averaged calcite distributions did not yield increased predictive strength for DMS concentrations in our analysis (see Sect. 2.6). However, as satellite PIC preferentially reflects the optical signature of detached coccoliths, monthly-averaged satellite PIC observations may represent the senescence of coccolithophore blooms, rather than active growth phases. Additionally, applying a chlorophyll-a based taxonomic algorithm (Hirata et al., 2011; Zeng et al., 2018) yielded no further explanation of the DMS variability predicted. The influence of taxonomic composition thus remains cryptic within our modelling framework.

4.2 Implications of Improved Predictive Power

As noted above, both the RFR and ANN approaches demonstrate significantly improved accuracy over existing models, explaining up to 62% of observed DMS variability (Fig. 2, 3). This predictive skill is somewhat lower than that achieved for methane fluxes (Weber et al., 2019) and dissolved inorganic carbon dynamics (Roshan and DeVries, 2017), where R^2 values ranging from 0.7 to 0.95 were obtained. Nonetheless, the dramatic accuracy improvement of our algorithms over traditional methods (Fig. 2, 3) encourages the further use of these techniques in modelling DMS distributions.

Improved predictive accuracy provides opportunities to gain insight into the mechanisms driving DMS cycling. Our approach has yielded accurate DMS predictions at a 4 to 40-fold higher resolution than previous algorithms (Simó and Dachs, 2002; Vallina and Simó, 2007; Galí et al., 2018; Watanabe et al., 2007), enabling the description of mesoscale patterns and processes (Fig. 8). Extending these methods to sub-mesoscale resolution will enable investigations into the dependence of DMS on finer-scale hydrographic processes, particularly stratification and frontal dynamics, which have been increasingly linked to DMS cycling but remain unresolved mechanistically (Royer et al., 2015; Asher et al., 2011). Moreover, coupling machine learning algorithms with biophysical and tracer export models holds promise to resolve the contributions of eddy dynamics and upwelling intensity on DMS variability, likely through nutrient availability and physiological mechanisms (Asher et al., 2011; Bailey et al., 2008; Cullen et al., 2009). Recent work has also developed a new database of DMS apparent quantum yields (Galí et al., 2016). As the availability of these measurements increases, simultaneous mapping of both DMS quantum yields and concentrations will become feasible, enabling future studies to better parse out the contribution of photolysis, physical mixing, and biological drivers of DMS cycling.

Although used in a diagnostic capacity here, our statistical models also hold potential for prognostic applications. Frameworks utilizing shorter time scales will likely be able to detect underlying mechanisms

508 driving observed diel cycling (Galí et al., 2013; Royer et al., 2016), even if the underlying mechanisms are still
509 unresolved. We note, however, that caution will need be exercised as machine learning models have a tendency
510 to overfit noise (Weber et al., 2019; Roshan and DeVries, 2017; Wang et al., 2020), thus requiring appropriately
511 large training datasets and the use of known “future” observations to validate predictive accuracy in this context.
512 The significant variability in DMS cycling across oceanic regimes will likely also render predictions more
513 successful at regional, rather than global, scales (Galí et al., 2018; Royer et al., 2015). Nonetheless, prognostic
514 applications of these algorithms should be investigated to aid in the future development of improved mechanistic
515 models.

516 **5 Conclusions**

517 We have presented a statistical approach for modelling DMS distributions, which provides significantly
518 higher predictive skill than traditional methods (Simó and Dachs, 2002; Vallina and Simó, 2007; Galí et al., 2018;
519 Watanabe et al., 2007; Lana et al., 2011), and yields estimates of the summertime NESAP DMS sea-air fluxes to
520 1.16 ± 1.22 Tg S in agreement with previous findings (Herr et al., 2019; Lana et al., 2011). Our results further
521 underscore the importance of the NESAP to global DMS production and motivate further observations in
522 traditionally under-sampled areas such as the Alaska Gyre and Aleutian Islands. Although we are unable to directly
523 examine the mechanistic drivers of DMS variability, our findings suggest nutrient limitation, light-driven
524 processes, and eddy-induced mixing are potentially key drivers of DMS cycling in the NESAP. Future studies will
525 benefit from using such statistical algorithms, in conjunction with field-based process studies and mechanistic
526 models, to better understand the underlying dynamics and driving factors in the oceanic DMS cycle.

527 *Code availability.* The analysis in this study makes extensive use of the Numpy, Matplotlib, & Scikit-Learn libraries
528 in Python. The custom codes used can be downloaded at
529 https://github.com/bjmcnabb/DMS_Climatology/tree/main/NESAP or are available upon request from the
530 corresponding author.

531 *Data Availability.* DMS observations and predictor datasets are described in the Methods with relevant links to
532 repositories. Data from the Lana et al. (2011) climatology used for comparison in Table 3 are available via the
533 SOLAs project (retrieved from www.bodc.ac.uk/solas_integration/implementation_products/group1/dms/), where
534 the DMS sea-air fluxes were calculated as described in Sect. 2.3. The gridded climatologies produced from each

535 algorithm in this study can be obtained at
536 https://github.com/bjmcnabb/DMS_Climatology/tree/main/NESAP/Climatologies.

537 *Author Contribution.* BM and PT designed the study. Model code was written and implemented by BM. BM
538 prepared the manuscript with significant contributions from PT.

539 *Competing Interests.* The authors declare that they have no conflict of interest.

540 *Acknowledgements.* We would like to thank Dr. Valentina Radic for her advice in model design and four
541 anonymous reviewers for their helpful comments that improved this manuscript. This work was supported by grants
542 to BM and PT from the Natural Sciences and Engineering Research Council of Canada (NSERC).

543

544 References

- 545 Allen, A. E., LaRoche, J., Maheswari, U., Lommer, M., Schauer, N., Lopez, P. J., Finazzi, G., Fernie, A. R., and
 546 Bowler, C.: Whole-cell response of the pennate diatom *Phaeodactylum tricornutum* to iron starvation,
 547 *Proceedings of the National Academy of Sciences*, 105, 10438–10443, <https://doi.org/10/cs9k8x>, 2008.
- 548 Archer, S. D., Ragni, M., Webster, R., Airs, R. L., and Geider, R. J.: Dimethyl sulfoniopropionate and dimethyl
 549 sulfide production in response to photoinhibition in *Emiliana huxleyi*, *Limnology and Oceanography*, 55, 1579–
 550 1589, <https://doi.org/10/dvpwqb>, 2010.
- 551 Asher, E. C., Merzouk, A., and Tortell, P. D.: Fine-scale spatial and temporal variability of surface water
 552 dimethylsulfide (DMS) concentrations and sea–air fluxes in the NE Subarctic Pacific, *Marine Chemistry*, 126, 63–
 553 75, <https://doi.org/10/chmbhk>, 2011.
- 554 Asher, E. C., Dacey, J. W., Ianson, D., Peña, A., and Tortell, P. D.: Concentrations and cycling of DMS, DMSP,
 555 and DMSO in coastal and offshore waters of the Subarctic Pacific during summer, 2010–2011, *J. Geophys. Res.*
 556 *Oceans*, 122, 3269–3286, <https://doi.org/10.1002/2016JC012465>, 2017.
- 557 Ayers, G. P. and Cainey, J. M.: The CLAW hypothesis: a review of the major developments, *Environ. Chem.*, 4,
 558 366, <https://doi.org/10/b7p54b>, 2007.
- 559 Bailey, K. E., Toole, D. A., Blomquist, B., Najjar, R. G., Huebert, B., Kieber, D. J., Kiene, R. P., Matrai, P.,
 560 Westby, G. R., and del Valle, D. A.: Dimethylsulfide production in Sargasso Sea eddies, *Deep Sea Research Part*
 561 *II: Topical Studies in Oceanography*, 55, 1491–1504, <https://doi.org/10/fnqb6j>, 2008.
- 562 Bates, T. S., Lamb, B. K., Guenther, A., Dignon, J., and Stoiber, R. E.: Sulfur emissions to the atmosphere from
 563 natural sources, *J Atmos Chem*, 14, 315–337, <https://doi.org/10/chmgt6>, 1992.
- 564 Behrenfeld, M. J. and Falkowski, P. G.: Photosynthetic rates derived from satellite-based chlorophyll
 565 concentration, *Limnology and Oceanography*, 42, 1–20, <https://doi.org/10/cg5x4k>, 1997.
- 566 Behrenfeld, M. J. and Milligan, A. J.: Photophysiological Expressions of Iron Stress in Phytoplankton, *Annu.*
 567 *Rev. Mar. Sci.*, 5, 217–246, <https://doi.org/10.1146/annurev-marine-121211-172356>, 2013.
- 568 Behrenfeld, M. J., Westberry, T. K., Boss, E. S., O'Malley, R. T., Siegel, D. A., Wiggert, J. D., Franz, B. A.,
 569 McClain, C. R., Feldman, G. C., Doney, S. C., Moore, J. K., Dall'Olmo, G., Milligan, A. J., Lima, I., and
 570 Mahowald, N.: Satellite-detected fluorescence reveals global physiology of ocean phytoplankton,
 571 *Biogeosciences*, 6, 16, <https://doi.org/10/fdn3f2>, 2009.
- 572 Bell, T. G., De Bruyn, W., Miller, S. D., Ward, B., Christensen, K. H., and Saltzman, E. S.: Air–sea
 573 dimethylsulfide (DMS) gas transfer in the North Atlantic: evidence for limited interfacial gas exchange at high
 574 wind speed, *Atmos. Chem. Phys.*, 13, 11073–11087, <https://doi.org/10.5194/acp-13-11073-2013>, 2013.
- 575 Belviso, S., Sciandra, A., and Copin-Montégut, C.: Mesoscale features of surface water DMSP and DMS
 576 concentrations in the Atlantic Ocean off Morocco and in the Mediterranean Sea, *Deep Sea Research Part I:*
 577 *Oceanographic Research Papers*, 50, 543–555, [https://doi.org/10.1016/S0967-0637\(03\)00032-3](https://doi.org/10.1016/S0967-0637(03)00032-3), 2003.

578 Blomquist, B. W., Brumer, S. E., Fairall, C. W., Huebert, B. J., Zappa, C. J., Brooks, I. M., Yang, M., Bariteau,
579 L., Prytherch, J., Hare, J. E., Czerski, H., Matei, A., and Pascal, R. W.: Wind Speed and Sea State Dependencies
580 of Air-Sea Gas Transfer: Results From the High Wind Speed Gas Exchange Study (HiWinGS), 122, 8034–8062,
581 <https://doi.org/10/gcmxd3>, 2017.

582 Bock, J., Michou, M., Nabat, P., Abe, M., Mulcahy, J. P., Olivié, D. J. L., Schwinger, J., Suntharalingam, P.,
583 Tjiputra, J., van Hulten, M., Watanabe, M., Yool, A., and Séférian, R.: Evaluation of ocean dimethylsulfide
584 concentration and emission in CMIP6 models, *Biogeosciences*, 18, 3823–3860, <https://doi.org/10/gk6fw8>, 2021.

585 Bouillon, R.-C. and Miller, W. L.: Determination of apparent quantum yield spectra of DMS photo-degradation
586 in an in situ iron-induced Northeast Pacific Ocean bloom: AQY of DMS in an iron-induced bloom, *Geophys.*
587 *Res. Lett.*, 31, n/a-n/a, <https://doi.org/10/d96wkn>, 2004.

588 Bouillon, R.-C. and Miller, W. L.: Photodegradation of Dimethyl Sulfide (DMS) in Natural Waters: Laboratory
589 Assessment of the Nitrate-Photolysis-Induced DMS Oxidation, *Environ. Sci. Technol.*, 39, 9471–9477,
590 <https://doi.org/10/d2j84c>, 2005.

591 Boyd, P. and Harrison, P. J.: Phytoplankton dynamics in the NE subarctic Pacific, *Deep Sea Research Part II:*
592 *Topical Studies in Oceanography*, 46, 2405–2432, <https://doi.org/10/fkg4mz>, 1999.

593 Boyd, P. W., Law, C. S., Wong, C. S., Nojiri, Y., Tsuda, A., Levasseur, M., Takeda, S., Rivkin, R., Harrison, P.
594 J., Strzepek, R., Gower, J., McKay, R. M., Abraham, E., Arychuk, M., Barwell-Clarke, J., Crawford, W.,
595 Crawford, D., Hale, M., Harada, K., Johnson, K., Kiyosawa, H., Kudo, I., Marchetti, A., Miller, W., Needoba, J.,
596 Nishioka, J., Ogawa, H., Page, J., Robert, M., Saito, H., Sastri, A., Sherry, N., Soutar, T., Sutherland, N., Taira,
597 Y., Whitney, F., Wong, S.-K. E., and Yoshimura, T.: The decline and fate of an iron-induced subarctic
598 phytoplankton bloom, *Nature*, 428, 549–553, <https://doi.org/10/fkgnf4>, 2004.

599 Brieman, L.: *Random Forests*, 45, 5–32, 2001.

600 Brimblecombe, P. and Shooter, D.: Photo-oxidation of dimethylsulphide in aqueous solution, *Marine Chemistry*,
601 19, 343–353, <https://doi.org/10/bqwp9>, 1986.

602 Bucciarelli, E., Ridame, C., Sunda, W. G., Dimier-Hugueney, C., Cheize, M., and Belviso, S.: Increased
603 intracellular concentrations of DMSP and DMSO in iron-limited oceanic phytoplankton *Thalassiosira oceanica*
604 and *Trichodesmium erythraeum*, *Limnology and Oceanography*, 58, 1667–1679,
605 <https://doi.org/10.4319/lo.2013.58.5.1667>, 2013.

606 Byrd, R. H., Lu, P., Nocedal, J., and Zhu, C.: A Limited Memory Algorithm for Bound Constrained
607 Optimization, *SIAM J. Sci. Comput.*, 16, 1190–1208, <https://doi.org/10/bpjm24>, 1995.

608 Charlson, R. J., Lovelock, J. E., Andreae, M. O., and Warren, S. G.: Oceanic phytoplankton, atmospheric
609 sulphur, cloud albedo and climate, *Nature*, 326, 655–661, <https://doi.org/10.1038/326655a0>, 1987.

610 Cullen, J. T., Chong, M., and Ianson, D.: British Columbian continental shelf as a source of dissolved iron to the
611 subarctic northeast Pacific Ocean, *Global Biogeochem. Cycles*, 23, <https://doi.org/10/b489x8>, 2009.

- 612 Dacey, J. W. H. and Wakeham, S. G.: Oceanic Dimethylsulfide: Production During Zooplankton Grazing on
613 Phytoplankton, *Science*, 233, 1314–1316, <https://doi.org/10.1126/science.233.4770.1314>, 1986.
- 614 Dickson, D. M. J. and Kirst, G. O.: Osmotic Adjustment in Marine Eukaryotic Algae: The Role of Inorganic Ions,
615 Quaternary Ammonium, Tertiary Sulphonium and Carbohydrate Solutes, *New Phytologist*, 106, 645–655,
616 <https://doi.org/10.1111/j.1469-8137.1987.tb00165.x>, 1987.
- 617 Fiechter, J. and Moore, A. M.: Iron limitation impact on eddy-induced ecosystem variability in the coastal Gulf of
618 Alaska, *Journal of Marine Systems*, 92, 1–15, <https://doi.org/10/bvqv4d>, 2012.
- 619 Franklin, D., Steinke, M., Young, J., Probert, I., and Malin, G.: Dimethylsulphoniopropionate (DMSP), DMSP-
620 lyase activity (DLA) and dimethylsulphide (DMS) in 10 species of coccolithophore, *Mar. Ecol. Prog. Ser.*, 410,
621 13–23, <https://doi.org/10/fk7hmj>, 2010.
- 622 Freeland, H. J., Crawford, W. R., and Thomson, R. E.: Currents along the pacific coast of Canada, *Atmosphere-
623 Ocean*, 22, 151–172, <https://doi.org/10.1080/07055900.1984.9649191>, 1984.
- 624 Galí, M., Simó, R., Vila-Costa, M., Ruiz-González, C., Gasol, J. M., and Matrai, P.: Diel patterns of oceanic
625 dimethylsulfide (DMS) cycling: Microbial and physical drivers, *Global Biogeochem. Cycles*, 27, 620–636,
626 <https://doi.org/10.1002/gbc.20047>, 2013.
- 627 Galí, M., Kieber, D. J., Romera-Castillo, C., Kinsey, J. D., Devred, E., Pérez, G. L., Westby, G. R., Marrasé, C.,
628 Babin, M., Levasseur, M., Duarte, C. M., Agustí, S., and Simó, R.: CDOM Sources and Photobleaching Control
629 Quantum Yields for Oceanic DMS Photolysis, *Environ. Sci. Technol.*, 50, 13361–13370,
630 <https://doi.org/10/f9jg2w>, 2016.
- 631 Galí, M., Levasseur, M., Devred, E., Simó, R., and Babin, M.: Sea-surface dimethylsulfide (DMS) concentration
632 from satellite data at global and regional scales, *Biogeosciences*, 15, 3497–3519, <https://doi.org/10/gdrn6n>, 2018.
- 633 Garcia, H. E., Weathers, K. W., Paver, C. R., Smolyar, I., Boyer, T. P., Locarnini, M. M., Zweng, M. M.,
634 Mishonov, A. V., Baranova, O. K., and Seidov, D.: World Ocean Atlas 2018. Vol. 4: Dissolved Inorganic
635 Nutrients (phosphate, nitrate and nitrate+ nitrite, silicate), 35pp., 2019.
- 636 Gardner, M. W. and Dorling, S. R.: Artificial neural networks (the multilayer perceptron)—a review of
637 applications in the atmospheric sciences, *Atmospheric Environment*, 32, 2627–2636, <https://doi.org/10/ft4hjb>,
638 1998.
- 639 Goddijn-Murphy, L., Woolf, D. K., and Marandino, C.: Space-based retrievals of air-sea gas transfer velocities
640 using altimeters: Calibration for dimethyl sulfide, 117, <https://doi.org/10/gm8ngj>, 2012.
- 641 Green, D. H., Shenoy, D. M., Hart, M. C., and Hatton, A. D.: Coupling of Dimethylsulfide Oxidation to Biomass
642 Production by a Marine Flavobacterium, *Appl. Environ. Microbiol.*, 77, 3137–3140, <https://doi.org/10/cp6r33>,
643 2011.
- 644 Hatton, A. D. and Wilson, S. T.: Particulate dimethylsulphoxide and dimethylsulphoniopropionate in
645 phytoplankton cultures and Scottish coastal waters, *Aquat. Sci.*, 69, 330–340, <https://doi.org/10/dbxk6n>, 2007.

646 Hatton, A. D., Shenoy, D. M., Hart, M. C., Mogg, A., and Green, D. H.: Metabolism of DMSP, DMS and DMSO
647 by the cultivable bacterial community associated with the DMSP-producing dinoflagellate *Scrippsiella*
648 *trochoidea*, *Biogeochemistry*, 110, 131–146, <https://doi.org/10/ggnh23>, 2012.

649 Hegg, D. A., Radke, L. F., and Hobbs, P. V.: Measurements of Aitken nuclei and cloud condensation nuclei in
650 the marine atmosphere and their relation to the DMS-Cloud-climate hypothesis, *J. Geophys. Res. Atmos.*, 96,
651 18727–18733, <https://doi.org/10/d6fwx9>, 1991.

652 Herr, A. E., Kiene, R. P., Dacey, J. W. H., and Tortell, P. D.: Patterns and drivers of dimethylsulfide
653 concentration in the northeast subarctic Pacific across multiple spatial and temporal scales, *Biogeosciences*, 16,
654 1729–1754, <https://doi.org/10.5194/bg-16-1729-2019>, 2019.

655 Herr, A. E., Dacey, J. W. H., Kiene, R. P., McCulloch, R. D., Schuback, N., and Tortell, P. D.: Potential roles of
656 dimethylsulfoxide in regional sulfur cycling and phytoplankton physiological ecology in the NE Subarctic Pacific,
657 *Limnology and Oceanography*, <https://doi.org/10/ghfstm>, 2020.

658 Hirata, T., Hardman-Mountford, N. J., Brewin, R. J. W., Aiken, J., Barlow, R., Suzuki, K., Isada, T., Howell, E.,
659 Hashioka, T., Noguchi-Aita, M., and Yamanaka, Y.: Synoptic relationships between surface Chlorophyll-a and
660 diagnostic pigments specific to phytoplankton functional types, *Biogeosciences*, 8, 311–327,
661 <https://doi.org/10.5194/bg-8-311-2011>, 2011.

662 Humphries, G. R. W., Deal, C. J., Elliott, S., and Huettmann, F.: Spatial predictions of sea surface
663 dimethylsulfide concentrations in the high arctic, *Biogeochemistry*, 110, 287–301, <https://doi.org/10/fx778z>,
664 2012.

665 Kiene, R. P. and Linn, L. J.: The fate of dissolved dimethylsulfoniopropionate (DMSP) in seawater: Tracer
666 studies using ³⁵S-DMSP, *Geochimica et Cosmochimica Acta*, 64, 2797–2810, [https://doi.org/10.1016/S0016-](https://doi.org/10.1016/S0016-7037(00)00399-9)
667 [7037\(00\)00399-9](https://doi.org/10.1016/S0016-7037(00)00399-9), 2000.

668 Kinsey, J. D., Kieber, D. J., and Neale, P. J.: Effects of iron limitation and UV radiation on *Phaeocystis antarctica*
669 growth and dimethylsulfoniopropionate, dimethylsulfoxide and acrylate concentrations, *Environ. Chem.*, 13,
670 195–211, <https://doi.org/10.1071/EN14275>, 2016.

671 Kirst, G. O., Thiel, C., Wolff, H., Nothnagel, J., Wanzek, M., and Ulmke, R.: Dimethylsulfoniopropionate
672 (DMSP) in icealgae and its possible biological role, *Marine Chemistry*, 35, 381–388,
673 [https://doi.org/10.1016/S0304-4203\(09\)90030-5](https://doi.org/10.1016/S0304-4203(09)90030-5), 1991.

674 Korhonen, H., Carslaw, K. S., Spracklen, D. V., Mann, G. W., and Woodhouse, M. T.: Influence of oceanic
675 dimethyl sulfide emissions on cloud condensation nuclei concentrations and seasonality over the remote Southern
676 Hemisphere oceans: A global model study, *J. Geophys. Res. Atmos.*, 113, <https://doi.org/10/cfrz46>, 2008.

677 Ksionzek, K. B., Lechtenfeld, O. J., McCallister, S. L., Schmitt-Kopplin, P., Geuer, J. K., Geibert, W., and Koch,
678 B. P.: Dissolved organic sulfur in the ocean: Biogeochemistry of a petagram inventory, *Science*, 354, 456–459,
679 <https://doi.org/10.1126/science.aaf7796>, 2016.

680 Lana, A., Bell, T. G., Simó, R., Vallina, S. M., Ballabrera-Poy, J., Kettle, A. J., Dachs, J., Bopp, L., Saltzman, E.
681 S., Stefels, J., Johnson, J. E., and Liss, P. S.: An updated climatology of surface dimethylsulfide concentrations
682 and emission fluxes in the global ocean, *Global Biogeochem. Cycles*, 25, <https://doi.org/10/dbqjrm>, 2011.

683 Levasseur, M., Scarratt, M. G., Michaud, S., Merzouk, A., Wong, C. S., Arychuk, M., Richardson, W., Rivkin, R.
684 B., Hale, M., Wong, E., Marchetti, A., and Kiyosawa, H.: DMSP and DMS dynamics during a mesoscale iron
685 fertilization experiment in the Northeast Pacific-Part I: Temporal and vertical distributions, *Deep Sea Research*
686 Part II: Topical Studies in Oceanography, 53, 2353–2369, <https://doi.org/10.1016/j.dsr2.2006.05.023>, 2006.

687 Li, Z. and Cassar, N.: Satellite estimates of net community production based on O₂/Ar observations and
688 comparison to other estimates, *Global Biogeochem. Cycles*, 30, 735–752, <https://doi.org/10/f8v6bh>, 2016.

689 Lidbury, I., Kröber, E., Zhang, Z., Zhu, Y., Murrell, J. C., Chen, Y., and Schäfer, H.: A mechanism for bacterial
690 transformation of dimethylsulfide to dimethylsulfoxide: a missing link in the marine organic sulfur cycle,
691 *Environ. Microbiol.*, 18, 2754–2766, <https://doi.org/10.1111/1462-2920.13354>, 2016.

692 Lizotte, M., Levasseur, M., Michaud, S., Scarratt, M. G., Merzouk, A., Gosselin, M., Pommier, J., Rivkin, R. B.,
693 and Kiene, R. P.: Macroscale patterns of the biological cycling of dimethylsulfoniopropionate (DMSP) and
694 dimethylsulfide (DMS) in the Northwest Atlantic, *Biogeochemistry*, 110, 183–200, <https://doi.org/10/fx9svt>,
695 2012.

696 Mahowald, N. M., Engelstaedter, S., Luo, C., Sealy, A., Artaxo, P., Benitez-Nelson, C., Bonnet, S., Chen, Y.,
697 Chuang, P. Y., Cohen, D. D., Dulac, F., Herut, B., Johansen, A. M., Kubilay, N., Losno, R., Maenhaut, W.,
698 Paytan, A., Prospero, J. M., Shank, L. M., and Siefert, R. L.: Atmospheric Iron Deposition: Global Distribution,
699 Variability, and Human Perturbations, *Annu. Rev. Mar. Sci.*, 1, 245–278, <https://doi.org/10/fsn8tj>, 2009.

700 Malin, G., Wilson, W. H., Bratbak, G., Liss, P. S., and Mann, N. H.: Elevated production of dimethylsulfide
701 resulting from viral infection of cultures of *Phaeocystis pouchetii*, *Limnology and Oceanography*, 43, 1389–1393,
702 <https://doi.org/10/bw7vjf>, 1998.

703 Martin, J. H. and Fitzwater, S. E.: Iron deficiency limits phytoplankton growth in the north-east Pacific subarctic,
704 *Nature*, 331, 341–343, <https://doi.org/10/bvtg6v>, 1988.

705 Merzouk, A., Levasseur, M., Scarratt, M. G., Michaud, S., Rivkin, R. B., Hale, M. S., Kiene, R. P., Price, N. M.,
706 and Li, W. K. W.: DMSP and DMS dynamics during a mesoscale iron fertilization experiment in the Northeast
707 Pacific-Part II: Biological cycling, 53, 2370–2383, <https://doi.org/10.1016/j.dsr2.2006.05.022>, 2006.

708 Nelson, N. B. and Siegel, D. A.: The Global Distribution and Dynamics of Chromophoric Dissolved Organic
709 Matter, *Annu. Rev. Mar. Sci.*, 5, 447–476, <https://doi.org/10/dcwcbk>, 2013.

710 Nemcek, N., Ianson, D., and Tortell, P. D.: A high-resolution survey of DMS, CO₂, and O₂/Ar distributions in
711 productive coastal waters, *Global Biogeochem. Cycles*, 22, 1–13, <https://doi.org/10.1029/2006gb002879>, 2008.

712 Nevitt, G. A.: Sensory ecology on the high seas: the odor world of the procellariiform seabirds, *Journal of*
713 *Experimental Biology*, 211, 1706–1713, <https://doi.org/10/d2rdz3>, 2008.

714 Nightingale, P. D., Malin, G., Law, C. S., Watson, A. J., Liss, P. S., Liddicoat, M. I., Boutin, J., and Upstill-
 715 Goddard, R. C.: In situ evaluation of air-sea gas exchange parameterizations using novel conservative and
 716 volatile tracers, *Global Biogeochem. Cycles*, 14, 373–387, <https://doi.org/10/d9dztz>, 2000.

717 Okkonen, S. R., Jacobs, G. A., Joseph Metzger, E., Hurlburt, H. E., and Shriver, J. F.: Mesoscale variability in
 718 the boundary currents of the Alaska Gyre, *Continental Shelf Research*, 21, 1219–1236, <https://doi.org/10/dc2n79>,
 719 2001.

720 Roshan, S. and DeVries, T.: Efficient dissolved organic carbon production and export in the oligotrophic ocean,
 721 *Nat Commun*, 8, 2036, <https://doi.org/10/gcrfdg>, 2017.

722 Royer, S.-J., Levasseur, M., Lizotte, M., Arychuk, M., Scarratt, M. G., Wong, C. S., Lovejoy, C., Robert, M.,
 723 Johnson, K., Peña, A., Michaud, S., and Kiene, R. P.: Microbial dimethylsulfoniopropionate (DMSP) dynamics
 724 along a natural iron gradient in the northeast subarctic Pacific, 55, 1614–1626, <https://doi.org/10/ch6cqb>, 2010.

725 Royer, S.-J., Galí Tàpias, M., Saltzman, E., McCormick, C., Bell, T., and Simó, R.: Development and validation
 726 of a shipboard system for measuring high-resolution vertical profiles of aqueous dimethylsulfide concentrations
 727 using chemical ionisation mass spectrometry, *Environmental Chemistry*, <https://doi.org/10/f6c3qp>, 2014.

728 Royer, S.-J., Mahajan, A. S., Galí, M., Saltzman, E., and Simó, R.: Small-scale variability patterns of DMS and
 729 phytoplankton in surface waters of the tropical and subtropical Atlantic, Indian, and Pacific Oceans, *Geophys.*
 730 *Res. Lett.*, 42, 475–483, <https://doi.org/10/gkxzf6>, 2015.

731 Royer, S.-J., Galí, M., Mahajan, A. S., Ross, O. N., Pérez, G. L., Saltzman, E. S., and Simó, R.: A high-resolution
 732 time-depth view of dimethylsulphide cycling in the surface sea, *Sci. Rep.*, 6, 32325,
 733 <https://doi.org/10.1038/srep32325>, 2016.

734 Saltzman, E. S., Bruyn, W. J. D., Lawler, M. J., Marandino, C. A., and McCormick, C. A.: A chemical ionization
 735 mass spectrometer for continuous underway shipboard analysis of dimethylsulfide in near-surface seawater,
 736 *Ocean Sci.*, 10, <https://doi.org/10/bv59ng>, 2009.

737 Schmidtko, S., Johnson, G. C., and Lyman, J. M.: MIMOC: A global monthly isopycnal upper-ocean climatology
 738 with mixed layers, *J. Geophys. Res. Oceans*, 118, 1658–1672, <https://doi.org/10/ggqp4h>, 2013.

739 Sheehan, C. E. and Petrou, K.: Dimethylated sulfur production in batch cultures of Southern Ocean
 740 phytoplankton, *Biogeochemistry*, 147, 53–69, <https://doi.org/10/ghjqgm>, 2020.

741 Simó, R. and Dachs, J.: Global ocean emission of dimethylsulfide predicted from biogeophysical data, *Global*
 742 *Biogeochem. Cycles*, 16, 26-1-26–10, <https://doi.org/10/cmqkh2>, 2002.

743 Simó, R. and Vila-Costa, M.: Ubiquity of algal dimethylsulfoxide in the surface ocean: Geographic and temporal
 744 distribution patterns, *Marine Chemistry*, 100, 136–146, <https://doi.org/10/bg5bph>, 2006.

745 Slezak, D., Brugge, A., and Herndl, G.: Impact of solar radiation on the biological removal of
 746 dimethylsulfoniopropionate and dimethylsulfide in marine surface waters, *Aquat. Microb. Ecol.*, 25, 87–97,
 747 <https://doi.org/10/ftjwjd>, 2001.

- 748 Spiese, C. and Tatarkov, E.: Dimethylsulfoxide reduction activity is linked to nutrient stress in *Thalassiosira*
 749 *pseudonana* NCMA 1335, *Mar. Ecol. Prog. Ser.*, 507, 31–38, <https://doi.org/10.3354/meps10842>, 2014.
- 750 Spiese, C. E., Kieber, D. J., Nomura, C. T., and Kiene, R. P.: Reduction of dimethylsulfoxide to dimethylsulfide
 751 by marine phytoplankton, *Limnology and Oceanography*, 54, 560–570,
 752 <https://doi.org/10.4319/lo.2009.54.2.0560>, 2009.
- 753 Stefels, J.: Physiological aspects of the production and conversion of DMSP in marine algae and higher plants,
 754 *Journal of Sea Research*, 43, 183–197, [https://doi.org/10.1016/S1385-1101\(00\)00030-7](https://doi.org/10.1016/S1385-1101(00)00030-7), 2000.
- 755 Steiner, N. S., Robert, M., Arychuk, M., Levasseur, M. L., Merzouk, A., Peña, M. A., Richardson, W. A., and
 756 Tortell, P. D.: Evaluating DMS measurements and model results in the Northeast subarctic Pacific from 1996–
 757 2010, *Biogeochemistry*, 110, 269–285, <https://doi.org/10/b99pfb>, 2012.
- 758 Strzepek, R. F. and Harrison, P. J.: Photosynthetic architecture differs in coastal and oceanic diatoms, *Nature*,
 759 431, 689–692, <https://doi.org/10/fk2fs7>, 2004.
- 760 Sunda, W. G., Kieber, D., and Kiene, R. P.: An antioxidant function of DMSP and DMS in marine algae Oceanic
 761 dimethylsulfide (DMS) photolysis, *Nature*, 418, 317–320, <https://doi.org/10.1038/nature00851>, 2002.
- 762 Taalba, A., Xie, H., Scarratt, M. G., Bélanger, S., and Levasseur, M.: Photooxidation of dimethylsulfide (DMS)
 763 in the Canadian Arctic, *Biogeosciences*, 10, 6793–6806, <https://doi.org/10/f5jhsv>, 2013.
- 764 Toole, D. A., Slezak, D., Kiene, R. P., Kieber, D. J., and Siegel, D. A.: Effects of solar radiation on
 765 dimethylsulfide cycling in the western Atlantic Ocean, *Deep Sea Research Part I: Oceanographic Research*
 766 *Papers*, 53, 136–153, <https://doi.org/10/bret7m>, 2006.
- 767 Tortell, P. D.: Dissolved gas measurements in oceanic waters made by membrane inlet mass spectrometry,
 768 *Limnology and Oceanography: Methods*, 3, 24–37, <https://doi.org/10/drmjv5>, 2005a.
- 769 Tortell, P. D.: Small-scale heterogeneity of dissolved gas concentrations in marine continental shelf waters,
 770 *Geochemistry, Geophysics, Geosystems*, 6, <https://doi.org/10/bgqvs9>, 2005b.
- 771 del Valle, D. A., Kieber, D. J., Bisgrove, J., and Kiene, R. P.: Light-Stimulated Production of Dissolved DMSO
 772 by a Particle-Associated Process in the Ross Sea, Antarctica, *Limnology and Oceanography*, 52, 2456–2466,
 773 <https://doi.org/10.4319/lo.2007.52.6.2456>, 2007.
- 774 Vallina, S. M. and Simó, R.: Strong relationship between DMS and the solar radiation dose over the global
 775 surface ocean, *Science*, 315, 506–508, <https://doi.org/10.1126/science.1133680>, 2007.
- 776 Vance, T., Davidson, A., Thomson, P., Levasseur, M., Lizotte, M., Curran, M., and Jones, G.: Rapid DMSP
 777 production by an Antarctic phytoplankton community exposed to natural surface irradiances in late spring, *Aquat.*
 778 *Microb. Ecol.*, 71, 117–129, <https://doi.org/10/gmw5hv>, 2013.

779 Vila-Costa, M., Valle, D. A. D., González, J. M., Slezak, D., Kiene, R. P., Sánchez, O., and Simó, R.:
 780 Phylogenetic identification and metabolism of marine dimethylsulfide-consuming bacteria, 8, 2189–2200,
 781 <https://doi.org/10.1111/j.1462-2920.2006.01102.x>, 2006.

782 Wang, W.-L., Song, G., Primeau, F., Saltzman, E. S., Bell, T. G., and Moore, J. K.: Global ocean dimethyl
 783 sulfide climatology estimated from observations and an artificial neural network, *Biogeosciences*, 17, 5335–5354,
 784 <https://doi.org/10/ghn33p>, 2020.

785 Watanabe, Y. W., Yoshinari, H., Sakamoto, A., Nakano, Y., Kasamatsu, N., Midorikawa, T., and Ono, T.:
 786 Reconstruction of sea surface dimethylsulfide in the North Pacific during 1970s to 2000s, *Marine Chemistry*,
 787 103, 347–358, <https://doi.org/10/bzz33z>, 2007.

788 Webb, A. L., van Leeuwe, M. A., den Os, D., Meredith, M. P., J. Venables, H., and Stefels, J.: Extreme spikes in
 789 DMS flux double estimates of biogenic sulfur export from the Antarctic coastal zone to the atmosphere, *Sci.*
 790 *Rep.*, 9, 2233, <https://doi.org/10/ghjqgc>, 2019.

791 Weber, T., Wiseman, N. A., and Kock, A.: Global ocean methane emissions dominated by shallow coastal
 792 waters, *Nat. Commun.*, 10, 4584, <https://doi.org/10/gf9pc7>, 2019.

793 Westberry, T. K., Behrenfeld, M. J., Milligan, A. J., and Doney, S. C.: Retrospective satellite ocean color analysis
 794 of purposeful and natural ocean iron fertilization, *Deep Sea Research Part I: Oceanographic Research Papers*, 73,
 795 1–16, <https://doi.org/10/f4rcbn>, 2013.

796 Westberry, T. K., Shi, Y. R., Yu, H., Behrenfeld, M. J., and Remer, L. A.: Satellite-Detected Ocean Ecosystem
 797 Response to Volcanic Eruptions in the Subarctic Northeast Pacific Ocean, *Geophys. Res. Lett.*, 46, 11270–11280,
 798 <https://doi.org/10/ggr9ms>, 2019.

799 Whitney, F. A., Crawford, W. R., and Harrison, P. J.: Physical processes that enhance nutrient transport and
 800 primary productivity in the coastal and open ocean of the subarctic NE Pacific, *Deep Sea Research Part II:*
 801 *Topical Studies in Oceanography*, 52, 681–706, <https://doi.org/10/dkn9sn>, 2005.

802 Yang, S., Chang, B. X., Warner, M. J., Weber, T. S., Bourbonnais, A. M., Santoro, A. E., Kock, A., Sonnerup, R.
 803 E., Bullister, J. L., Wilson, S. T., and Bianchi, D.: Global reconstruction reduces the uncertainty of oceanic
 804 nitrous oxide emissions and reveals a vigorous seasonal cycle, *Proc Natl Acad Sci USA*, 117, 11954–11960,
 805 <https://doi.org/10/ghc3hw>, 2020.

806 Zavarisky, A., Goddijn-Murphy, L., Steinhoff, T., and Marandino, C. A.: Bubble-Mediated Gas Transfer and Gas
 807 Transfer Suppression of DMS and CO₂, 123, 6624–6647, <https://doi.org/10.1029/2017JD028071>, 2018.

808 Zeng, C., Rosengard, S. Z., Burt, W., Peña, M. A., Nemcek, N., Zeng, T., Arrigo, K. R., and Tortell, P. D.:
 809 Optically-derived estimates of phytoplankton size class and taxonomic group biomass in the Eastern Subarctic
 810 Pacific Ocean, *Deep Sea Research Part I: Oceanographic Research Papers*, 136, 107–118,
 811 <https://doi.org/10.1016/j.dsr.2018.04.001>, 2018.

812